A DIFFERENTIAL REQUIREMENT FOR THE CILIOPATHY GENE *RPGRIP1L* IN HUMAN AND MOUSE SPINAL PROGENITOR FATE SPECIFICATION

Antonia Wiegering[1,*], Isabelle Anselme[1], Ludovica Brunetti[1], Laura Metayer-Derout[1], Damelys Calderon[2], Sophie Thomas[2], Stéphane Nedelec[3], Alexis Eschstruth[1], Sylvie Schneider-Maunoury[1,*], Aline Stedman[1,*]

[1] Sorbonne Université, Institute of Biology Paris-Seine, CNRS UMR 7622, Inserm U1156, Paris, France.

[2] INSERM UMR 1163, Institut Imagine, Université Paris Cité, Paris, France.

[3] Sorbonne Université, Institut du Fer à Moulin, Inserm UMR-S 1270, Paris France

*co-senior authors, co-corresponding authors

ABSTRACT

Studying developmental processes in the context of the human central nervous system is essential to understand neurodevelopmental diseases. In this paper we perform a comparative functional study of the ciliopathy gene *RPGRIP1L* in human and mouse spinal development using in vitro 3D differentiation of pluripotent stem cells. *RGPRIP1L*, a causal gene of severe neurodevelopmental ciliopathies such as Joubert and Meckel syndromes, encodes a scaffolding protein of the ciliary transition zone involved in ciliary gating. Previous work has identified a major role for *Rpgrip1l* in mouse brain and spinal cord development, via controlling the Sonic Hedgehog (SHH)/GLI pathway. We show that spinal organoids derived from *Rpgrip1l* mutant mouse embryonic stem cells faithfully recapitulate the loss of motoneurons and the strong reduction of SHH signaling observed in the mutant mice. In contrast, human induced pluripotent stem cells mutant for *RPGRIP1L* produce motoneurons and activate the SHH pathway at levels similar to wild types. Moreover, we show that, in human *RPGRIP1L* mutant organoids, MNs acquire a more anterior identity, expressing *HOX* genes and proteins normally present in the hindbrain while motoneurons from wild type organoids strictly display spinal identity. By performing a temporal transcriptome analysis throughout the differentiation process, we find that the anteroposterior specification defect arises in early axial progenitors. Thus, this study uncovers distinct functions in humans and mice for a ciliopathy protein and a novel role for RPGRIP1L in human spinal anteroposterior patterning. These findings have important implications for understanding the role of cilia in human spinal cord development and the pathogenic mechanisms of neurodevelopmental ciliopathies.

INTRODUCTION

Primary cilia are highly conserved signaling organelles that protrude from the surface of most vertebrate cells. Constructed from a microtubule scaffold, the ciliary axoneme is anchored in the plasma membrane via the basal body, a modified mother centriole. Since cilia are not separated from the rest of the cell by a membrane like other organelles, a specific structure above the basal body, the so-called ciliary transition zone (TZ), regulates the entry and exit of proteins, thereby acting as a "ciliary gate" that regulates the composition of cilia and creates an independent cell compartment. By exerting sensory functions such as SHH, WNT and PDGFR signaling transduction, cilia play essential roles in embryonic development and adult tissue homeostasis. Consequently, defects in primary cilia function can lead to a large group of genetically and phenotypically heterogeneous syndromes called ciliopathies (1, 2).

Interestingly, although ubiquitously present, mutations in ciliary genes lead to very diverse pathologies that can affect organs like the retina, kidneys, lung, heart and the central nervous system (CNS) whereby the symptoms caused by ciliary mutations greatly vary based on the mutated gene but also between patients. Nonetheless, some correlations can be drawn between groups of mutated genes based on their localization, possibly their function and the ciliopathy syndrome to which they lead. Although this is not completely deterministic, mutations in genes encoding ciliary TZ proteins often lead to neurodevelopmental ciliopathies such as Joubert Syndrome (JS) and the embryonically lethal Meckel Gruber syndrome (MKS) (1, 3). It was demonstrated that primary cilia are present throughout the neuronal lineage, from neural stem to progenitor cells, mature neurons and glia, where they play an essential role in CNS formation by modulating signaling pathways and cell cycle progression (4-10). Most of the current knowledge about neurodevelopmental defects in ciliopathy patients and their underlying mechanisms was gained by analyzing *in vivo* and *in vitro* animal models. Using these approaches, we and others have demonstrated that the JS causative gene *RPGRIP1L* encodes a large scaffolding protein acting as a keystone of TZ construction (11-26). In addition, it regulates proteasomal activity at the ciliary base and autophagy in murine cells (27, 28) and is involved in planar cell polarity in zebrafish (29). Furthermore, an essential function for Rpgrip1l in SHH signaling was demonstrated in mouse embryonic tissues and cultured cells (11, 15, 16, 30). However, our understanding of the role of Rpgrip1l and other ciliary proteins in human neural fate is still very partial and has been hampered due to the paucity of human models, limiting our ability to understand the role of cilia in the human development, and the origin of neural developmental defects in ciliopathies. Moreover, evidence suggests that primary cilia function could be only partially overlapping between human and animal models, partly due to specificities in human CNS development. For example, while *Rpgrip1l* mutant mouse embryos, like other ciliary mutants, display a severe disorganization of the diencephalic, hypothalamic regions and the spinal cord, no such phenotype was described in ciliopathy patients (6, 7, 31-33).

In this study, we took advantage of pluripotent stem cell-based organoids approaches to study the role of RPGRIP1L in human neural progenitor (NP) fate. Since spinal organoids models from mouse and

human pluripotent stem cells are well characterized, and the role for ciliary proteins in SHH-dependent patterning of the ventral spinal cord has been largely studied, we used WT and Rpgrip1l-deficient mouse embryonic stem cell (mESC)- and human induced pluripotent stem cell (hiPSC)-derived spinal organoids to compare the cell-intrinsic functions of RPGRIP1L in ciliogenesis and spinal progenitors between these two models. We show that mouse *Rpgrip1l-/-* organoids exhibit altered dorso-ventral patterning in response to SHH, similar to mutant mouse embryos, emphasizing the cell-intrinsic requirement for Rpgrip1l in spinal progenitors for cilia-dependent SHH pathway activation and commitment into ventral neuronal cell types. In contrast, RPGRIP1L-deficient human iPSCs submitted to a similar differentiation protocol are still able to form primary cilia and adopt SHH-dependent ventral spinal fates. Most importantly, we uncover a new role for the human ciliary RPGRIP1L protein in the precise allocation of antero-posterior identities of spinal progenitors, with a shift of mutant MNs from thoracic to more rostral/hindbrain identities that originates in early neuromesodermal progenitors. With this study, we bring a first proof of concept that inter-species differences can be dissected by dynamically comparing mouse and human ex vivo organoids and we highlight new human-specific functions for the ciliopathy gene *RPGRIP1L* in antero-posterior patterning of axial progenitors.

RESULTS

Rpgrip1l KO mouse spinal organoids faithfully recapitulate the murine *Rpgrip1l* KO phenotype and present defective SHH-induced motoneuron specification

In vertebrates, graded SHH signaling along the ventro-dorsal axis of the spinal cord is necessary for the specification of the five different ventral progenitor domains p3, pMN, p2, p1 and p0 (Figure 1B) (34-41). The study of mouse ciliary mutant embryos demonstrated that primary cilia are required for SHH transduction and the correct establishment of spinal DV patterning (15, 42-45). In *Rpgrip1l*$^{-/-}$ (KO) mouse embryos, primary cilia are absent in the developing spinal cord neural tube and brain (15, 16), coinciding with a strong reduction of SHH expression in the notochord and with its absence from the FP region at embryonic stage (E)11.5 (6, 15). As a consequence, the FP and p3 territories are not established, fewer pMNs are specified and the dorsal identities are shifted ventrally. In order to test whether this phenotype can be reproduced *ex vivo*, even under conditions where SHH activation is forced by the addition of a constant dose of SHH agonist (Smoothened AGonist, SAG), we established WT and Rpgrip1l KO mESC lines from mouse blastocysts that we differentiated into ventral spinal organoids adapting already validated differentiation protocols (Figure 1A) (46-47). Briefly, mESC-derived embryoid bodies (EBs) grown in N2B27 neuralizing medium during 2 days are directed into spinal ventral identities by addition of the Wnt agonist CHIR99021, SAG and retinoic acid (RA). EBs are then let to differentiate for 5 to 7 days. Differentiated spinal organoids were collected at different time points, sectioned and immunostained to assess the identity of the different spinal progenitors obtained. We found that approximately 50% of spinal progenitors from control organoids committed to a pMN fate by day 4 of the differentiation, as evidenced by Olig2 staining (Figure 1C-E). pMNs progressively differentiated into post-mitotic MNs until day 6, a stage when Olig2 staining could not be detected anymore, but Islet1 positive MNs could be observed (Figure 1C, E). Control organoids were also composed of progenitors from the more ventral domains p3 and FP since we could detect the presence of [Nkx6.1+, Olig2-], Nkx2.2+ and FoxA2+ cells (Figure 1D-F). Moreover, control organoids nicely recapitulated the sequential activation of ventral neural identities observed *in vivo* in the mouse spinal cord, as *Olig2* expression preceded the initiation of *Nkx2.2* and *FoxA2*. In contrast, *Rpgrip1l*-deficient spinal organoids failed to commit to ventral spinal identities, and switched to a more dorsal fate since we observed a strong decrease in the number of Olig2, Nkx2.2 and Nkx6.1-expressing neural progenitors, both by immunostaining for these transcription factors (Figure 1A-F), and by RT-qPCR assessing for their RNA expression (Figure S1). To gain a more global view of the changes in cell fate occurring in mutant organoids, we performed bulk RNAseq from 3 independent experiments of differentiation, on control and mutant organoids from day 2 to day 7 (Figure S1). Our transcriptomic analysis confirmed the shift towards dorsal identities in *Rpgrip1l* mutant organoids, and showed that SHH-dependent ventral cell types were replaced by progenitors expressing markers characteristics of the p0-P2 domains such as *Dbx1* (Figure 1G). Consistently, the molecular signature of post-mitotic neurons changed from V3-MNs in the control, to V1-V0 (Figure 1H) in *Rpgrip1l* KO organoids. The

temporal analysis of *Isl1* and *Tuj1* expression in the time course of the differentiation (Figure 1I, J), showed that the reduction in MNs correlated with a transient decrease in neurogenesis between days 3 and 7 in *Rpgrip1l* KO compared with control organoids. Since MNs are the first neurons to differentiate in the spinal cord, this result is in line with the dorsalization occurring in the mutant organoids. Altogether, these results show that *Rpgrip1l* KO spinal organoids phenotype faithfully recapitulate the defects described *in vivo*, in mouse mutant embryos. They also underline that the absence of ventral identities observed in the mouse is the consequence of intrinsic defects of spinal progenitors rather than an indirect consequence of the loss of SHH signaling from the notochord.

In *Rpgrip1l* mutant mice, the defective patterning of the ventral spinal cord has been attributed to an absence of primary cilia in spinal progenitors, and the consequent defect in SHH pathway activation (6, 15). To test whether it could also be the case *ex vivo* in our organoid system, we analyzed the ciliary markers Arl13b and Ift88 by immunostaining on organoid sections. We found that similar to what was observed *in vivo*, *Rpgrip1l* deficiency leads to a drastic reduction of the ciliary Arl13b amount (Figure 2A, B). This phenotype might reflect a ciliary gating defect, or an absence of ciliary axoneme. To discriminate between these 2 scenarios, we analyzed the axonemal protein Ift88 and measured the length of Ift88 staining as a way to evaluate the axonemal length. We found that the axoneme of mutant progenitors was abnormally stunted, with a mean length of 0.2 µm compared to 1 µm in the control (Figure 2A, C), suggesting that only the TZ might be present overlying the basal body. This ciliary phenotype was correlated with the complete absence of Rpgrip1l at the ciliary TZ in mutant organoids (Figure 2A). Finally, since PCs are required for SHH signaling and the absence of ventral spinal progenitors is reminiscent of a defective SHH pathway, we assessed the activation of the SHH pathway in control and KO organoids in our transcriptomic data (Figure 2D-F). The expression of direct targets of the pathway was globally decreased in the mutant (Figure 2 D). *Gli1*, *Patched1* and *Hhip* were upregulated in controls from day 2, upon SAG addition into the EB culture medium, their expression barely increased in the mutants, showing impaired activation of SHH transduction in absence of Rpgrip1l (Figure 2D-F). Overall, our results demonstrate that, as *in vivo*, Rpgrip1l is required *in vitro* in mouse spinal progenitors for ciliogenesis, SHH pathway activation and the consequent acquisition of spinal ventral identities. These results provide the first proof of concept that spinal organoids differentiated from pluripotent stem cells (PSCs) constitute a good model to study the consequences of ciliary genes deletions on neural cell fate.

Human RPGRIP1L deficient neural progenitors differentiate into MNs in spinal organoids

To tackle the function of primary cilia and the TZ protein RPGRIP1L in human spinal development and SHH transduction, we generated human iPSC clones deficient for RPGRIP1L (*RPGRIP1L*$^{-/-}$) via introduction of *InDel* mutations that lead to premature STOPs in two independent hiPSC lines (Figure S2). Validated clones from both hiPSC lines (Ph2 and Wtc11; Figure S2) were used for differentiation into ventral spinal organoids following a well-established 3D differentiation protocol (Figure 3A) (48,

49). An additional clone, carrying a full deletion of RPGRIP1L (Δexon3-exon27), was used as a control (Figure S2). To gain a global view of the dynamic changes in cell fate occurring in mutant organoids, we performed bulk RNAseq on WT and RPGRIP1L-deficient organoids from two independent experiments of differentiation. In total, we collected material from two control clones of the Ph2 hiPSC line and the Wtc11 hiPSC line each (WT: n=4) and from two RPGRIP1L-deficient clones of the Ph2 hiPSC line and 1 RPGRIP1L-deficient clone of the Wtc11 hiPSC line (KO: n=3) (Figure S4). Importantly, both hiPSC lines behaved the same in terms of differentiation efficiency, cilia phenotype and gene expression profiles (Figure S3, S4). For immunofluorescence analyses, two WT and two RPGRIP1L-deficient clones of the Ph2 hiPSC line and two control and two RPGRIP1L-deficient clones of the Wtc11 hiPSC line were analyzed for each experiment (WT: n=4, KO: n=4) (Figure S2). Starting the differentiation of ventral spinal organoids from single cell hiPSCs, EBs were formed after one day in a floating culture in neural induction medium (dual SMAD inhibition) containing the GSK3-beta antagonist CHIR99021 for moderate WNT activation (Figure 3A). Within four days, WT and RPGRIP1L-deficient cells adopted a caudal (axial) fate indicated by TBXT/BRACHYURY, CDX2 and SOX2 expression (Figure 6A-C and Figure S3A). These axial progenitors can give rise to mesodermal and neuroectodermal structures and are therefore also called neuromesodermal progenitors (NMPs) (50-54). From day 4 onwards, axial progenitors were treated with RA and high concentrations of SAG in order to induce a ventral neural fate (Figure 3A). At day 6 of ventral spinal organoid differentiation, the majority of control and RPGRIP1L-deficient cells expressed SOX2 and PAX6, both markers of early NPs, indicating that control cells as well as RPGRIP1L-deficient cells adopted the neural fate (Figure S3B). From day 6 onwards, SOX2 and PAX6 expression decreased corresponding to the ongoing specification and differentiation process. In response to SAG stimulation, the MN progenitor marker OLIG2 started to be expressed between day 4 and day 6 of differentiation with an expression peak reached at day 9 where 75% of the cells within organoids expressed OLIG2 (Figure 3B, C and Figure S3C). Combined to that, cells expressed the broad ventral marker NKX6.1 at day 9 of differentiation, further evidence of ventral spinal fate specification (Figure S3C). Surprisingly, no difference in OLIG2 and NKX6.1 pattern was observed between control and RPGRIP1L-deficient organoids (Figure 3B, C and Figure S3C). In line with this, control and RPGRIP1L-deficient cells started to express *ISL1* and *ISL2*, markers for postmitotic MNs, from day 9 onwards (Figure S3F, G). A final treatment of organoids with a Gamma-Secretase Inhibitor (DAPT) was used to inhibit NOTCH signaling and accelerate the neural differentiation into postmitotic MNs from day 9 onwards (Figure 3A). Consequently, ISL1/2 RNA and protein levels were strongly upregulated within WT and RPGRIP1L-deficient organoids between day 11 and day 14 (Figure 3B and Figure S3F, G). Taken together, these results show that RPGRIP1L-deficient hiPSCs are able to correctly process differentiation from stem cells to NPs and further from pMNs to postmitotic MNs. Nevertheless, our data reveal 10-20 % less ISL1/2-positive MNs at the end of differentiation in RPGRIP1L-deficient hiPSC-derived spinal organoids compared to control situations (Figure 3B).

By analyzing the expression of various transcription factors that are distinctly expressed in specific dorso-ventral regions of the developing spinal cord, we tested whether, despite the normal pMN production, human iPSC-derived organoids deficient for RPGRIP1L exhibited a slight shift in dorso-ventral patterning towards the dorsal domains, as it was demonstrated for mESC-derived *Rpgrip1l* KO spinal organoids (Figure 1). The unaltered expression of the broad ventral marker *NKX6.1* (Figure 3C and Figure S3C), the intermediate marker *DBX1* and *DBX2* (Figure 3C), and the dorsal spinal marker *PAX3* , *PAX7* , and *ZIC1* (Figure 3C) during differentiation, indicated that, contrary to mouse Rpgrip1l-deficient spinal organoids, human RPGRIP1L-deficient spinal organoids did not display a more dorsal progenitor type specification.

To investigate whether the mildly reduced number of MNs in RPGRIP1L-deficient organoids could be caused by a delayed neurogenesis, we analyzed the expression of the global neuronal markers *TUBB3* and *MAP2* . As expected, expression of both markers increased during differentiation with the highest expression of *TUBB3* and *MAP2* between day 11 and day 14 (Figure 3E and Figure S3H) and high protein levels of TUBB3 at day 14 (Figure 3E). Comparing WT and RPGRIP1L-deficient organoids, no significant differences between *MAP2* and *TUBB3* expression on RNA or protein level could be observed. In conclusion, neurogenesis appears unaltered and seems not to be responsible for the reduced number of MNs observed in RPGRIP1L-deficient spinal organoids.

Surprisingly, NKX2.2 RNA and protein expression was significantly increased at day 11 of MN differentiation in RPGRIP1L-deficient cells (Figure 3C, D). NKX2.2 is expressed in a specific subpopulation of ventral spinal MN progenitors in humans (55), where it is co-expressed with OLIG2. By performing co-labeling of OLIG2 and NKX2.2 at day 9 and day 11 of differentiation we could not detect any increase in OLIG2/NKX2.2 double positive cells in RPGRIP1L-deficient organoids compared to WT controls (Figure 3D and Figure S3E). Consequently, the increased NKX2.2 amount in RPGRIP1L-deficient spinal organoids is unlikely to be caused by increased numbers of ventral and human-specific MN subtypes. NKX2.2 is also expressed in the most ventral NPs (p3) and neuronal subtype (V3) within the neural tube (Figure 1B). Here, expression of NKX2.2 plays a primary role in ventral neuronal patterning and requires high SHH signaling (56) raising the question about the status of SHH signaling in human RPGRIP1L-deficient spinal organoids.

RPGRIP1L deficient spinal neural progenitor possess cilia and transduce SHH signaling

Since differentiation into MNs is largely unaltered in control and RPGRIP1L-deficient hiPSC spinal organoids and the cells express high levels of the ventral gene *NKX2.2*, which depends on high SHH concentration, we hypothesized that cilia-mediated SHH signaling may be hyperfunctional in human spinal differentiation.

To determine SHH pathway activity in WT and RPGRIP1L-deficient spinal organoids, we analyzed the expression of SHH target genes *GLI1* and *PTCH1* along the entire spinal differentiation protocol using bulk RNAseq data. In both WT and RPGRIP1L-deficient spinal organoids, an increase in *GLI1* and

PTCH1 expression in response to SAG stimulation was observed between day 4 and day 9 of differentiation, followed by an expected decrease in their expression in accordance to the removal of SAG from the differentiation medium (Figure 4A). No significant difference in SHH target gene expression could be observed between WT and RPGRIP1L-deficient cells. This result is in line with the functional differentiation of RPGRIP1L-deficient hiPSCs into OLIG2 positive pMNs and ISL1/2 positive postmitotic MNs that depend on SHH signaling transduction (Figure 3C). In contrast, the earlier described increase in number of NKX2.2 positive cells in RPGRIP1L-deficient spinal organoids (Figure 3D, E and Figure S3E) cannot be explained by an increased SHH pathway activity and thus a ventralization effect in RPGRIP1L-deficient spinal organoids.

Based on the results of functional SHH transduction and MN differentiation in human RPGRIP1L-deficient spinal organoids, which are in complete contrast to the results of the mouse analyses, we expected RPGRIP1L-deficient spinal organoids to possess cilia. We analyzed cilia formation at day 6 of MN differentiation, a time point where organoids were stimulated with SAG in order to activate SHH signaling (Figure 3A) and adopted the pMN fate indicated by increase in OLIG2 expression as described above (Figure 3C). In WT organoids, short primary cilia were detectable on cells lining the outside or the inner lumen of the organoids, thereby pointing into the external environment or the internal cavities of the organoids (Figure 4B). These cilia were IFT81-positive and displayed a mean length of 1.3 µm (Figure 4C). RPGRIP1L was present at the ciliary transition zone in WT spinal organoids (Figure 4D). In RPGRIP1L-deficient organoids, RPGRIP1L was not detectable at the ciliary base (Figure 4D). Nevertheless, cilia were present lining apical surfaces (Figure 4B) and displaying a mean length of 1.3 µm as in WT (Figure 4C). However, while WT cilia accumulated the ciliary membrane markers ARL13B (ADP Ribosylation Factor Like GTPase 13B), INPP5E (Inositol Polyphosphate-5-Phosphatase E) and AC3 (Adenylate Cyclase 3), reduced amounts of ARL13B and AC3 but not INPP5E were observed in RPGRIP1L deficient cilia (Figure 4E, F). This indicates a disrupted ciliary gating in human spinal NPs upon RPGRIP1L deficiency. These results are in line with data from *c.elegans*, different mouse tissues and human cell lines, in which a disrupted TZ organization and in consequence an altered ciliary gating has been described under Rpgrip1l deficiency (19, 21, 23, 24, 57). Since ciliary gating can be involved in SHH signaling function (2, 17, 58) e.g. by regulating ciliary shuttling of pathway components such as SMO (Smoothened) thereby regulating ciliary GPR161 (G Protein-Coupled Receptor 161) amounts (59-61), we tested if GPR161-trafficking was disrupted in RPGRIP1L mutant spinal organoids. GPR161 was enriched in the ciliary membrane in SHH pathway-inactive WT and RPGRIP1L-deficient cells (Figure S3I). In WT and RPGRIP1L mutant NPs stimulated with SAG, GPR161 did not accumulate within the primary cilia and thus did not inhibit SHH pathway activation (Figure S3I). These results are in perfect agreement with the previously described functional SHH pathway activation in WT and RPGRIP1L-deficient spinal organoids and show that ciliary gating defects did not affect SHH signaling transduction in RPGRIP1L-deficient NPs.

RPGRIP1L-deficient spinal organoids show antero-posterior patterning defects

By analyzing the bulk RNASeq data of WT and RPGRIP1L-deficient spinal organoids at different time points during the 3D spinal differentiation in greater detail (Figure S4A), we mapped defects provoked by the loss of RPGRIP1L at different stages during human MN differentiation. By processing the RNASeq data, we could show that dynamic gene expression profiles from WT and RPGRIP1L-deficient organoids clustered together in a Principal Component Analysis (PCA) at each analyzed time point indicating unaltered timing of MN differentiation in RPGRIP1L-deficient organoids compared to controls (Figure S4B). Furthermore, by comparing WT and RPGRIP1L-deficient RNASeq data at each selected time point, only minor differences in gene expressions could be observed (Figure S4C) and testing for overrepresented gene categories via gene ontology (GOSEQ) analyses did not reveal any significant changes in biological processes, molecular functions or cellular components between WT and RPGRIP1L-deficient samples at different time points. These results demonstrate that no major defects between WT and RPGRIP1L-deficient NPs, WT and RPGRIP1L-deficient spinal pMNs and WT and RPGRIP1L-deficient MNs exist in our model. Interestingly, among the few genes that were differentially expressed between WT and RPGRIP1L-deficient organoids, expression of *HOX* genes such as *HOXC6* and *HOXA7* were significantly downregulated in RPGRIP1L-deficient organoids at day 11 and day 14 (Figure S4D). In addition to this significant downregulation of *HOX* genes at late stages, *Ensemble of Gene Set Enrichment Analyses* (EGSEA) provided evidence for an altered HOX code in RPGRIP1L-deficient organoids at early and late stages (Figure S3E). EGSEA on GeneSetDB gene ontology (GO) at day 2 and on GeneSetDB Disease/Phenotype at day 2, day 4, day 11 and day 14 of differentiation, revealed significant downregulation for the GO term of the biological process *anterior/posterior pattern specification* (GO:0009952) at day 2 (Figure S4E) and the disease phenotype *abnormal rib attachment* (MPO gsdb4505) at day 2, day 4, day 11 and day 14 of differentiation (Figure S4F). All gene lists contain downregulation of HOX genes such as *HOXA9*, *HOXB6*, *HOXB8*, *HOXB9*, *HOXC6*, *HOXC8*, and *HOXC9*.

The HOX code is a central element of axial patterning and *HOX* genes are expressed in four clusters, HOX-A, HOX-B, HOX-C and HOX-D, along the rostro-caudal axis of bilateral organisms (Figure 5D). In humans, HOX proteins are encoded by 39 genes whose regionalized expression is realized by their sequential and collinear activation in axial progenitors, which gradually give rise to mesodermal and neuroectodermal structures with rostral and later caudal identity, each expressing a specific HOX code (49, 53, 54, 62, 63).

By analyzing the dynamic expression pattern of the 4 *HOX* gene clusters over time, we identified early established differences in the expression of posterior *HOX* genes in RPGRIP1L-deficient organoids compared to controls. In control organoids, early axial progenitors at day 2 started to express anterior HOX genes such as *HOXA1* followed by induction of later and more posterior HOX gene expressions such as *HOXC8* at day 4 of differentiation (Figure 5A, B). At later stages, WT organoids expressed anterior as well as more posterior *HOX* genes of the four different clusters such as HOX-A genes from

HOXA1 to *HOXA7* and HOX-C genes from *HOXC1* to *HOXC8* (Figure 5A, B). Corresponding to this expression code, MNs within WT organoids adopted a thoracic antero-posterior identity that could be visualized by immunofluorescence labeling of HOXC8, a marker for thoracic positions at day 14 (Figure 5C). In contrast, MNs in WT organoids did not translate anterior HOX proteins such as HOXA5 that would rather indicate a cervical/hindbrain positioning (Figure 5C). During early stages of differentiation, RPGRIP1L-deficient axial progenitors expressed anterior *HOX* genes comparable to the WT situation while expression of later and more posterior *HOX* genes was already reduced at day 4 (Figure 5A, B). This reduced expression was strikingly visible at later stages, where the latest HOX genes expressed in RPGRIP1L-deficient MNs were *HOXA5* instead of *HOXA7* and *HOXC4* instead of *HOXC8* (Figure 5A, B). This difference in HOX gene expression was confirmed by immunofluorescence, demonstrating that RPGRIP1L-deficient MNs do not express HOXC8 like the WT controls, but HOXA5 (Figure 5C). Taken together, the differences in *HOX* gene expression indicate a shift in antero-posterior patterning in RPGRIP1L-deficient organoids in which MNs adopt a more cervical/hindbrain identity specified by HOXA5 expression than a thoracic and spinal identity that can be observed in WT organoids (Figure 5D) (49, 62, 64). Interestingly, such antero-posterior patterning defect was specific to human spinal progenitors, since no altered expression of *Hox* genes could be identified in mutant organoids, neither in the transcriptome, nor in immunostainings for Hoxa5 and Hoxc6 (Figure S5).

RPGRIP1L-deficient spinal organoids adopt hindbrain MN identities

As discussed earlier, *NKX2.2* is expressed in the most ventral region of the neural tube (p3 and V3) and in human-specific ventral MNs (55), which we produce in small quantity in WT and RPGRIP1L-deficient human spinal organoids (Figure 3D, Figure S3E). Interestingly, it was demonstrated that *NKX2.2* is also expressed in MNs of the hindbrain (65-67). Studies in mouse and chick embryos showed that hindbrain MNs arise from NKX2.2-positive progenitors and that this lineage expresses additional markers such as *NKX2.9*, *PHOX2B* (65-71) and later on *TBX20* (69, 70, 72, 73). Since we demonstrated a clear anteriorization effect of MNs in RPGRIP1L-deficient spinal organoids indicated by altered *HOX* gene expression (Figure 5A-D), we hypothesized that the increase in *NKX2.2* expression (Figure 3C, D) corresponded to the generation of hindbrain rather than spinal MNs in RPGRIP1L-deficient organoids. Analyses of these markers revealed an increased expression of *PHOX2B* and *NKX2.9* upon RPGRIP1L-deficiency from day 6 of differentiation onwards (Figure 5E, F). In line with that, the late hindbrain-specific MN marker *TBX20* started to be expressed in RPGRIP1L-deficient organoids at day 11 and was highly expressed at day 14 (Figure 5G). Analyzing earlier markers of hindbrain-specific neural differentiation, the expression of *EGR2/KROX20* (70, 74-76) and *FGF3* (76-78) as well as the expression of the early hindbrain pMN marker *PHOX2A* (68, 70, 71) were strikingly increased in RPGRIP1L-deficient organoids at day 4 and day 2, respectively (Figure 5H, I, J). Taken together, our

results indicate that the disrupted antero-posterior patterning in RPGRIP1L-deficient organoids leads to the generation of hindbrain MNs instead of spinal MNs.

RPGRIP1L controls axial progenitor fate specification and early ciliogenesis in human spinal organoids

As detailed earlier, the sequential and collinear expression of HOX genes in human that lead to specification of rostral and later caudal identities is realized within axial progenitors (52-54, 62, 63, 79-83). In our organoid model, cells adopt the axial progenitor fate between day 2 and day 4 of differentiation indicated by coexpression of *CDX2*, *TBXT/BRACHYURY* and *SOX2* (Figure 6A, B, C and Figure S3A). Interestingly, *CDX2* and *TBXT/BRACHYURY* expression was reduced in RPGRIP1L-deficient organoids at early stages (Figure 6B, C) and labeling of CDX2 protein appeared patchy, with clusters of CDX2-negative cells in RPGRIP1L-deficient but not WT organoids at day 4 of differentiation (Figure 6A). These patterns of CDX2-negative cells were not detectable on all sections of RPGRIP1L-deficient organoids, leading to an unaltered overall CDX2-positive area per organoid in quantifications (Figure 6A). Moreover, while *TBXT/BRACHYURY* expression remained elevated between day 2 to day 4 in WT axial progenitors, it dropped as soon as day 2 in RPGRIP1L-deficient axial progenitors. In addition to CDX2 and TBXT/BRACHYURY, axial progenitors express the spinal cord-specific genes *CDX1* and *CDX4* (69, 84-90). Both *CDX* genes were expressed in WT spinal cord organoids, with *CDX1* being most highly expressed on day 2 and *CDX4* on day 4 of differentiation (Figure 6D, E). In contrast to that, induction of *CDX1* expression was strongly reduced and *CDX4* expression strikingly decreased in RPGRIP1L-deficient organoids (Figure 6D, E). During establishment of the axial progenitor pool, WNT/beta-Catenin and FGF signaling induce expression of early *HOX 1-4* genes as well as *CDX* gene expression (91, 92). Upon *CDX* gene expression, *CDX2* and *CDX4* mediate WNT/FGF induced expression of *HOX 5-9* genes (52, 86, 91, 93-97). In addition, WNT/beta-Catenin signaling in interaction with *CDX* genes induce *WNT5A* expression in axial progenitors (98, 99). Monitoring *WNT5A* expression levels in WT and RPGRIP1L-deficient spinal organoids, we found reduced *WNT5A* expression in RPGRIP1L-deficient spinal organoids at day 2 and more strikingly at day 4 of differentiation (Figure 6F). Thus, the loss of *CDX* and posterior *HOX* genes in RPGRIP1L-deficient organoids, as well as the abrupt decrease in *TBXT/BRACHYURY* expression, are suggestive of a decreased WNT signaling at the level of mutant axial progenitors.

Since primary cilia function was shown to be related to WNT/beta-Catenin signaling in certain cell types (100) as well as in the switch from canonical to non-canonical WNT signaling in xenopus larvae, mouse fibroblasts and human neural cell lines (101-104), we monitored the cilia status in WT and RPGRIP1L-deficient spinal organoids at day 4 of spinal cord differentiation. Surprisingly, we found a strong reduction in cilia number in RPGRIP1L-deficient organoids compared to controls (Figure 6G) which could provide an explanation for the reduced specification of axial progenitors and early anteroposterior defects shown above (Figure 6A-F). Remarkably, these results contrast with the ciliary

phenotype on NPs at day 6 of differentiation, where cilia were present on WT and on RPGRIP1L-deficient spinal organoids (Figure 4B, C). Consequently, our results indicated a cell-type specific function of RPGRIP1L in ciliogenesis during neural cell fate specification (Figure 5B, C).

DISCUSSION

Primary cilia are essential orchestrators of CNS development, but our current knowledge of their function in human neuronal development is still fragmentary, preventing a better understanding of the etiology of ciliopathies. In this study, we took advantage of PSCs derived spinal organoids to analyze the role of RPGRIP1L in both mouse and human spinal progenitors, enabling an unprecedented comparison of ciliary protein function between the two models. We find that, while in mouse, Rpgrip1l is required for the proper dorsoventral patterning of spinal progenitors, in human it regulates their anteroposterior identity. In addition, we uncover a species and cell type-specificity of cilia defects upon deficiency in a TZ protein. Our study has important implications for the role of cilia in human neural development and for understanding the region-specific defects in neurodevelopmental ciliopathies.

RPGRIP1L is differentially required for ciliogenesis and SHH activation in mouse and human ventral spinal progenitors

Previous analysis of the *Rpgrip1l* mutant mice demonstrated that deficiency for Rpgrip1l led to the absence of FP induction in mutant embryos, and to dorsoventral mis-patterning of the neural tube marked by the strong decrease of ventral neuronal subtypes like V3 and MNs. This phenotype was correlated to the absence of primary cilia and functional SHH signaling, and was also described for Ift mutant mice (15, 42-45). Since these mice are lacking a FP, a question remained as to whether altered patterning of the neural tube resulted only from the absence of SHH secretion ventrally, or from impairment of SHH signal transduction within ventral spinal progenitors. Here, by exposing control and *Rpgrip1l* mutant spinal organoids to high dose of SHH agonist, we show that primary cilia are intrinsically required within mouse spinal progenitors to transduce SHH. Upon inactive SHH signaling, mutant progenitors switch on intermediate-dorsal identities instead of ventral ones. Strikingly, we found that contrary to the mouse, human RPGRIP1L was not required for the establishment of ventral spinal neuronal cell types in organoids. Despite a clear ciliary gating defect, with decreased ARL13b or AC3 ciliary localization, human mutant spinal progenitors were still able to grow primary cilia and transduce SHH signaling similarly to controls, adopting MN identities. Ciliogenesis in the absence of Rpgrip1l has also been observed in other cellular contexts, like in mouse limbs progenitors, MEFs, HEK cells (23, 24, 27), or human fibroblasts derived from *RPGRIP1L* mutated JS patients (19). Whether the difference in ciliary phenotype observed between mouse and human spinal progenitors stems from differences in ciliary composition or stability, and accounts for the difference in SHH activation in these two systems remains to be addressed.

Progenitor-type specificity of cilia defects upon RPGRIP1L deficiency

More generally, in addition to the species-specificity discussed above, our results highlight a context-specific role for ciliary TZ proteins in neural progenitors in human RPGRIP1L-deficient organoids. While at day 6, NPs, most of which are already specified to the pMN fate, display cilia of normal length

and a moderately altered ciliary content, at day 4, neuromesodermal CDX2-positive progenitors display a strong reduction or loss of cilia number. Differences in ciliary structure and composition between tissues, already suggested by the high heterogeneity of phenotypes in human ciliopathies, has already been described in other models (23, 105-107). However, here we show for the first time a change in cilia sensitivity to the loss of a TZ protein along the process of neural progenitor specification in humans, at a key step of cell fate transition.

Whether this change parallels differences in ciliary structure, and which signaling and molecular cascades lead to these changes in cilia stability during the differentiation process are important questions raised by our study. In this regard, recent data show that cell fate can regulate ciliogenesis by different mechanisms such as transcriptional regulation (108), niche condition-specific regulation (109, 110), and several non-canonical signaling pathway activities such as SHH (111) and WNT (112). It will be an exciting future task to examine whether these modes of ciliogenesis regulation play a role in diverse spinal NPs and how RPGRIP1L is involved in it to explain at least in part the regional specificity of defects found in neurodevelopmental ciliopathies caused by mutations in *RPGRIP1L*.

Establishment of the HOX-code and regulation of antero-posterior patterning via RPGRIP1L

Quite unexpectedly, we found that although they do not display SHH-dependent dorsoventral patterning defects, human RPGRIP1L mutant spinal organoids shift to more anterior identities. Altered anteroposterior patterning could arise from several mechanisms. WNT, RA, Fibroblast Growth Factor (FGF), and more recently NOTCH signaling, were involved in the determination of axial progenitors and thereby regulation of gradual *HOX* gene expression (49, 69, 95, 113-116). From our transcriptome data, we could not observe any indication of perturbations in FGF or NOTCH pathways upon RPGRIP1L deficiency. However, we measured a reduced expression of *CDX2*, *CDX1* and *CDX4* as well as a downregulation of the *5-9 HOX* genes, detectable from the very early stages of the differentiation (Figure 5A, B, C, D). Analysis of Wnt3a- and Cdx-deficient mouse embryos (84, 97, 99, 117-121) or experimental manipulation of Cdx activity (121-124) lead to a working model in which early *CDX* expression activates and fine-tunes *HOX* gene expression profiles along the anterior-posterior axis downstream of WNT/beta-Catenin signaling in axial progenitors (52, 69, 80, 86, 91, 92, 95-97, 123-127). Interestingly, it was demonstrated recently that WNT signaling during early differentiation of hiPSCs into spinal MNs allows progressive, collinear HOX activation and that a switch to RA treatment at any time point during this process stops collinear HOX activation and favors transition into neuroectodermal progenitors with a discrete HOX gene profile (49, 95). Thus we hypothesize that the shift in antero-posterior patterning that we describe in RPGRIP1L-deficient human spinal organoids could result from reduced WNT transduction during early stages of axial progenitors differentiation, leading to a reduction in *CDX2*, *CDX1* and *CDX4* expression and the consequent decreased expression of posterior *HOX* genes, so that MNs adopt hindbrain rather than spinal identities.

At the current state of research, whether or not canonical WNT signaling is transduced by primary cilia remains controversial. Although some studies have demonstrated a localization of WNT signaling components in cilia or cilia proximity (101, 103) and a change in canonical WNT activity upon loss of cilia in certain cell types (100), other studies show that canonical WNT signaling functions independently of cilia (128). Recently, it was shown that non-canonical WNT signaling via GSK3-beta induces cilia formation in specific human cell lines (112). Moreover, Rpgrip1l regulates non-canonical WNT signaling via the prevention of dishevelled degradation in zebrafish, thereby modulating planar cell polarity processes (PCP) (29). Since WT and RPGRIP1L-deficient organoids are incubated at early stages of the differentiation protocol by the GSK3-beta inhibitor CHIR99021 to activate WNT signaling and induce axial fate (Figure 3A), it is most probable that WNT downregulation in the RPGRIP1L-deficient organoids takes place downstream of GSK3-beta. Therefore, the absence of primary cilia on RPGRIP1L-deficient spinal organoids at day 4 of differentiation might impact canonical and/or non-canonical WNT signaling, leading to the observed reduction in axial fate specification and MNs switch towards cervical/hindbrain identity instead of a spinal identity. With a still unknown mechanism, transient loss of PC in RPGRIP1L mutant axial progenitors could result in a decrease in WNT effectors at the level of *CDX* regulatory elements. Interestingly, chromatin occupancy of WNT/ß-Catenin effectors within mouse epiblast progenitors was shown to be dynamically regulated during mouse body plan formation, and influenced by Sox2 (129). Further analyses will show how cilia regulate WNT signaling and/or *CDX* gene expression during axial progenitor fate specification.

Relevance to the clinical features of ciliopathy patients

MNs play a pivotal role in human development. During prenatal life, their absence or degeneration generates a defect of fetal movements (fetal akinesia sequence) which eventually leads to malposition of joints (fetal akinesia deformation sequence) (130). The most frequent cause of prenatal spinal MN degeneration is type 0 spinal muscular atrophy (SMA) (131). In this study, we analyzed a gene that is responsible for Joubert and/or Meckel-Gruber syndromes (11-14) and to the best of our knowledge, prenatal spinal MN degeneration has never been reported in case of JS whatever the gene that is involved. Furthermore, no indications of ventral patterning defects or clinical signs of spinal motor dysfunction have been reported in human JS (32, 33), where an imbalance or motor phenotype have been mainly attributed to abnormalities in cerebellum or hindbrain development (1, 3). Post-mortem neuropathology of spinal cord in Joubert syndrome did not report any defect in the ventral spinal cord. Since the anteroposterior defects we observe seem to arise in early axial progenitors, which drive axial elongation of the embryo and participate to posterior tissues from the neck downward, we could also imagine that such anteroposterior defect might have a more general impact on development on axis elongation, and even impact the skeletal system. Subtle anterior homeotic transformations leading to defects in cranial skeletal structures have for example been observed in CDX1 mutant mice, with anomalies of the occipital bone (117, 132). Interestingly, one hallmark of Meckel syndrome is the

occipital encephalocele caused by defects in the occiput development (133). To dissect in more detail whether the antero-posterior patterning defect upon cilia gene mutation might be involved in development of patient phenotypes, further analysis of patient biopsies is needed. Complementary *in vitro* studies using ciliopathy patient-derived hiPSCs differentiated into spinal organoids should provide additional information.

MATERIAL and METHODS

mESCs culture and differentiation into ventral spinal organoids

mES cells were cultured in DMEM-GlutaMAX (Gibco) supplemented with 15% FCS, 100 µM β-mercaptoethanol, 100 U/ml penicillin, 0.1 mg/ml streptomycin, and 10^3 U/ml LIF (Millipore). To generate mouse spinal organoids, ESCs were dissociated and differentiated into embryoid bodies by seeding them in ultra-low attachment petri dishes (Corning) at a density of 9×10^4 cells ml^{-1} in N2B27 differentiation medium containing Advanced DMEMF12 and Neurobasal media (1:1, Life Technologies), B27 w/o vitamin A (Life Technologies), N2 (Life Technologies), 2 mM L-glutamine (Life Technologies), 0.1 mM β-mercaptoethanol, penicillin and streptomycin (Life Technologies). On day 2, the medium was changed and supplemented with 3µM CHIR, 10nM RA and 500nM SAG to induce ventral spinal fate. The medium was changed daily, with addition of 10nM RA only.

hiPSCs culture

hiPSCs were thawed in presence of Rock-inhibitor Y-27632 (5µM, Stemgent-Ozyme #04-0012) and cultured under standard conditions at 37°C in mTeSR+ medium (Stem Cell Technologies #100-0276) on Matrigel (Corning, VWR #354277) coated plates upon confluency of 70-80%. Passaging was performed using ReLeSR (Stem Cell Technologies #05872) and testing for potential mycoplasma contamination was performed regularly by Eurofins genomic (Mycoplasmacheck). Accutase (Stem Cell Technologies #07920) was used for the dissociation of hiPSC colonies into single cells.

Generation of mutant hiPSC lines

RPGRIP1L mutant and wildtype hiPSC clones were produced from two different hiPSC lines (PCIi033-A and UCSFi001-A) using CRISPR/Cas9 gene editing. The targeted exon 3 of RPGRIP1L and flanking sequences were sequenced prior to gene editing in both cell lines (see *on- and off-target analyses* section). The gRNA targeting exon 3 of *RPGRIP1L* was designed using the online design tool CRISPOR (134). Annealing of crRNA (Alt-R® CRISPR-Cas9 crRNA, 10 nmol, IDT) and tracrRNA (Alt-R® CRISPR-Cas9 tracrRNA, 20 nmol, IDT #1072533) was performed and 400.000 hiPSCs of each line were transfected with 1µl Cas9 protein (kindly provided by TACGENE, Paris, France) and 1µl gRNA (400 µM) using nucleofection. The transfected cells were cultured in mTeSR+ medium (Stem Cell Technologies #100-0276) containing Rock-inhibitor Y-27632 (10 µM, Stemgent-Ozyme #04-0012) for one day, replaced by mTeSR+ medium without Rock-inhibitor. Medium was changed every second day and serial dilutions were performed in mTeSR+ medium containing Rock-inhibitor Y-27632 and CloneR (1:1000, Stem Cell Technologies #05889). Rock-inhibitor was removed after two days and the medium containing CloneR was changed every second day until colonies were ready to be picked. Colonies were isolated in 24-well plates in mTesR+ medium containing CloneR. DNA was isolated for genotype analyses (see *on- and off-target analyses* section). Four WT (two clones of each

hiPSC line) and four homozygous mutant hiPSC clones (two of each hiPSC line) carrying *InDel* mutations that lead to premature STOP were used for further analyses (Figure S2). For the generation of additional RPGRIP1L-deficient hiPSC clones from the PCli033-A cell line we used a second strategy. We combined the gRNA targeting exon 3 of *RPGRIP1L* with a gRNA targeting exon 27 of *RPGRIP1L* to generate a full deletion of RPGRIP1L (Δexon3-exon27). This approach was performed at the ICV-iPS platform of the Brain Institute in Paris (ICM, Paris) under supervision of Stéphanie Bigou. One RPGRIP1L KO clone and one heterozygous control clone were used for further analyses (Figure S2).

Differentiation of hiPSCs into spinal organoids

Differentiation of wildtype and RPGRIP1L mutant hiPSCs was performed as previously described (48, 49). After amplification, hiPSC lines were dissociated into single cells using Accutase (Stem Cell Technologies #07920) and resuspended in differentiation medium N2B27 [vol:vol; Advanced DMEM/F-12 (Gibco) and Neurobasal Medium (Gibco)] supplemented with N2 (Thermo Fisher #17502048), B27 without Vitamin A (Thermo Fisher #12587010), penicillin/streptomycin 1 % (Thermo Fisher #15140122), β-mercaptoethanol 0.1 % (Thermo Fisher #31350010). Cells were seeded in a specific density of 1.5 x 10^5 cells/ml in ultra-low attachment dishes (Corning #3261) to allow embryoid body (EB) formation. The N2B27 differentiation medium was used throughout the whole differentiation process, but different additives were given at different time points (Figure 3A). Rock-inhibitor Y-27632 (5 µM; Stemgent-Ozyme #04-0012) was added from day 0 to day 2, CHIR-99021 (3 µM; Stemgent-Ozyme #04-0004) from day 0 to day 4, SB431542 (20 µM; Stemgent-Ozyme #04-0010) from day 0 to day 3 and LDN 193189 (0.1 µM; Stemgent-Ozyme #04-0074) from day 0 to day 4. The differentiation was preceded by adding Smoothened AGonist (SAG 500 nM; Merck #566660) and Retinoic Acid (100 nM RA; Sigma #R2625) to the N2B27 differentiation medium from day 4 to day 9. Gamma-Secretase inhibitor DAPT (10 µM; Tocris Bioscience #2634) was added from day 9 to the end of differentiation. Medium was changed every other day and additionally at day 3 of differentiation.

Embryoid body embedding and Cryosectioning

Murine and human spinal organoids were collected at different time points during differentiation, rinsed with PBS and fixed in cold PFA (4 %) for 7-12 min at 4 °C. EBs were rinsed in PBS and incubated in 30 % sucrose in PBS until completely saturated. Cryoprotected EBs were embedded in OCT embedding matrix (Cell Path #KMA-0100-00A) and stored at -80 °C. Cryostat sections were prepared and stored at -80 °C.

Immunofluorescence

Cryostat sections of murine and human EBs were washed in PBS/0.1% Triton X-100. Optional steps for permeabilization with PBS/0.5 %Triton X-100 for 10 min, post-fixation with MeOH (100 %) for 10

min or antigen-retrieval with Citrate-Buffer were performed depending on the antibody and specimen. After washing, cryosections were incubated with a blocking solution containing 10 % NGS in PBS/0.1% Triton-X100 for at least 2 hours. The sections were incubated with primary antibodies (Table S1) diluted in PBS/0.1 % Triton-X100 overnight at 4 °C. Next day, the slides were washed 3 x 5 min with PBS/0.1 % Triton-X100 and incubated with the secondary antibodies (Table S1) diluted in PBS/0.1 % Triton X-100 for 2 hours. After final washing steps with PBS/0.1 %Triton X-100 for at least 1 hour, sections were mounted with Vecta-Shield (Vector #H-1000) or Mowiol (Roth #0713.2) optionally containing DAPI (Merck #1.24653).

Image acquisition

Fluorescence image acquisition of patterning and differentiation markers was performed at room temperature using a Zeiss Observer Z1 equipped with an Apotome module, an Axiocam 506 monochrome cooled CCD camera and a 40x oil objective with a NA 1.3. All images were processed with Zen software (blue edition). Image analyses and figure preparation were performed using Fiji (ImageJ; National Institutes of Health). For cilia analyses, fluorescence images were acquired at room temperature using an inverted confocal microscope LSM 710 (Carl Zeiss AG), a 63x oil objective with a NA 1.4, and a monochrome charge-coupled device camera. Z-stacks with 0.2 µM steps were acquired. Images were processed with Zen software (black edition). Image analyses and figure preparation were performed using Fiji (ImageJ; National Institutes of Health).

STED images were acquired on the STEDYCON confocal and STED module (Abberior Instruments GmbH, Germany) connected to the lateral port of an IX83 inverted microscope (Evident Scientific). The STEDYCON SmartControl software was used for data acquisition. Imaging was performed using a UPLXAPO 100XO oil immersion objective (Evident Scientific). For STED, a pulsed 775 nm laser was used. STAR RED was excited with a pulsed 640 nm laser, STAR ORANGE was excited with a pulsed 561 nm laser, and DAPI was excited using a continuous wave 405nm source. Pixel size was 20 nm in xy direction, with a 250 nm step size in the z direction.

Quantification of fluorescent staining and statistical analyses

Fluorescent staining and protein band intensities were quantified using Fiji (ImageJ; National Institutes of Health). Intensity measurements of ciliary proteins was performed on unprocessed images (raw data) as described before (17, 23, 24, 27, 28, 58, 135, 136). After quantifications were performed, representative images were processed by means of background subtraction and contrast settings via Adobe Photoshop CS2.

For quantitative analyses of nuclear stainings, positive areas were defined and measured via setting specific thresholds in Fiji. For each image, the DAPI positive area (area 1) that corresponds to the area of the organoid was determined and measured. The area 2 corresponding to the marker of interest was determined and measured, too. By dividing area 2 by area 1, the percentage of the positive area for each

marker of interest per organoid slice was determined. At least 20 images per clone were used for area quantifications.

All data are presented as mean ± SEM. Two-tailed t test with Welch´s correction was performed for all data in which two datasets were compared. Two-tailed *t* test Analysis of variance (ANOVA) and Tukey honest significance difference (HSD) tests were used for all data in which more than two datasets were compared. $*P < 0.05$ was considered to be statistically significant, $**P < 0.01$ was defined as statistically very significant, and $***P < 0.001$ was noted as statistically high significant. All statistical data analysis and graph illustrations were performed by using GraphPad Prism (GraphPad Software).

RNA isolation and qPCR analyses

mESC- and hiPSC-derived organoids were collected at different stages during differentiation and washed with PBS. RNA was isolated using the RNeasy Kit (Qiagen #74104) and RNAse-free DNase Set (Qiagen #79254). Isolated RNA was transcribed into cDNA using the GoScript Reverse Transcriptase Kit (Promega #A5001). For quantitative real-time PCR, 50 ng of cDNA of each sample was used in a Maxima SYBR Green/ROX qPCR Master Mix 2x (Thermo Scientific #K0222). Triplicate reactions for each sample were prepared and the samples were run in a Step One Real-Time PCR Step One Real-Time PCR System Thermal Cycling Block (Applied Biosystems #4376357). The analysis of real-time data was performed using the included StepOne Software version 2.0 and graphs were generated using GraphPad Prism (GraphPad Software). Primer pairs are listed in Table S2.

Bulk RNAseq Analysis

mESC- and hiPSC-derived organoids were collected at different stages during differentiation and washed with PBS. For mouse organoids, samples from WT and *RPGRIP1L KO* were collected from 3 independent experiments. RNA was isolated using the RNeasy Kit (Qiagen #74104) and RNAse-free DNase Set (Qiagen #79254). RNA quality was determined by measuring the RNA integrity number (RIN) via the High Sensitive RNA Screen Tape Analysis kit (Agilent Technologies #5067) on the TapeStation system (Agilent Technologies). A RIN above 9.5 was considered as good quality RNA and 250 ng RNA in a total volume of 25 µl was prepared per sample for further procedure. Bulk RNAseq was realized by the Genotyping and Sequencing Core Facility of the Paris Brain Institute (iGenSeq, ICM Paris). RNAseq data processing was performed in Galaxy under supervision of the ARTBio platform (IBPS, Paris). Datasets were aligned against the *Mus_musculus.GRCm39.109* and the *homo sapiens.GRCh38.109* genome, respectively, by using the STAR alignment method (Galaxy Version 2.7.10b) (137). Quality of sequencing was controlled via MultiQC analyses (Galaxy Version 1.11) (138) and gene expression was assessed via featureCounts (Galaxy Version 2.0.3) (139). Tables listing the normalized expression values as Transcripts per Million (tpm) in log2(tpm+1) were created from raw count expression matrices via the Generate TPM tool (Galaxy Version 0.5.0). Principal Component Analyses (PCA) (Galaxy Version 0.9.6) (140) and heatmap analyses (Galaxy Version 3.1.3) were

performed based on the log2(tpm+1) data. For further analyses, differentially expressed genes (DEGs) were determined from featureCount tables by using the DESeq2 tool (Galaxy Version 2.11.40.7) (141). DESeq2 files were used for generation of Volcano Plots (Galaxy Version 0.0.5) (142) and goseq tests for overrepresented gene categories (Galaxy Version 1.50.0) (143). Additionally, easy and efficient ensembl gene set testing EGSEA (Ensemble of Gene Set Enrichment Analyses) analyses were performed on DESeq2 files (Galaxy Version 1.20.0) (144).

ACKNOWLEDGEMENT

Image acquisition was carried out at the IBPS Imaging Facility. We particularly thank Chloé Chaumeton from the IBPS imaging platform, and Frédéric Eghiaian from Abberior Instruments GmbH, for setting up the STED imaging. We also thank Christophe Antoniewski from the IBPS bioinformatics analyses platform ARTbio for the personal support on the RNAseq analysis, the ICV-iPS platform at the Paris Brain Institute (ICM) for the generation and characterization of RPGRIP1L-deficient hiPSC lines, and the iGenSeq sequencing platform at the ICM for reliable sequencing and fast processing of our samples. We are grateful to Vanessa Ribes and Pascal Gilardi Hebenstreit for providing us with protocols and help in PSCs culture and differentiation approaches. We also thank Martin Catala for bringing his expertise to bear in insightful discussions on the clinical aspects of neural ciliopathies. This work was supported by funding to SSM from the *Fondation pour la Recherche Médicale* (Equipe FRM EQU201903007943), from the *Fondation pour la Recherche sur le Cancer* (ARC; PJA 20171206591), from the *Agence Nationale de la Recherche* (ANR; ERA-NET Neuron project on neurodevelopmental disorders "NDCil"). AW received funding from the *German Research Foundation* (DFG; WI 5451/1-1). ST received funding from the *Agence Nationale de la Recherche* (ANR; ANR-17-CE16-0003-01 and ANR-17-RHUS-0002).

FIGURE LEGENDS

Figure 1: *Rpgrip1l*-deficient mouse spinal progenitors fail to adopt SHH-dependent ventral fates. **(A)** Schematic summary of the spinal 3D differentiation approach. Main neural progenitor and neuron populations obtained at each time point with their molecular markers are indicated below. Small molecules used to induce or repress signaling pathways are indicated above. CHIR: WNT agonist CHIR99021; SAG: SHH agonist; RA: Retinoic Acid. Modified after Maury et al., 2015. **(B)** Diagram depicting the main transcription factors spanning the different dorso-ventral progenitor (light blue) or neuronal (light green) domains of the developing spinal cord. **(C)** Immunofluorescence for Olig2 (pMN) and Islet1 (post-mitotic MNs) in sections from WT and Rpgrip1L-/- organoids at indicated time points. **(D)** Immunofluorescence for Nkx6-1 (p3-pMN-p2), Olig2 (pMN), Nkx2-2 (p3), FoxA2 (FP) and Pax6 (pMN-dp) in sections from WT and *Rpgrip1l*$^{-/-}$ organoids at indicated time points. **(E, F)** Quantification of the relative areas stained for the indicated markers in sections from WT and *Rpgrip1lL*$^{-/-}$ organoids at indicated time points. Data are shown as mean ± SEM. WT: n≥4; *RPGRIP1L*$^{-/-}$: n≥4. **(G, H)** Heatmaps of selected genes expressions in WT and *Rpgrip1l* deficient spinal organoids over time. WT: n=3; *RPGRIP1L*$^{-/-}$: n=3. **(K, L)** Temporal dynamics of *Isl1* and *Tuj1* expression analyzed in the course of differentiation. WT: n=3; *RPGRIP1L*$^{-/-}$: n=3. Data shown are mean±SEM. ***P < 0.001, ****P < 0.0001 (unpaired t tests with Welch´s correction). Scale bar, 50 µm.

Figure 2: Rpgrip1l-deficient mouse spinal organoids lack functional cilia and fail to activate the Shh pathway. **(A)** Immunofluorescence for the indicated ciliary markers on WT and Rpgrip1l-deficient spinal organoids at day 4 of differentiation. Cilia are present at apical sites pointing into inner cavities of the organoids. **(B, C)** Quantifications of ciliary stainings. Data shown are mean±SEM. WT: n=3; *RPGRIP1L*$^{-/-}$: n=3 **(D)** Heatmap of selected SHH targets in WT and *Rpgrip1l* deficient spinal organoids over time. **(E, F)** Temporal analysis of Gli1 and Patched1 expression in the course of the differentiation of WT and *Rpgrip1l*$^{-/-}$ organoids. Data shown are mean±SEM. WT: n=3; *RPGRIP1L*$^{-/-}$: n=3. ***P < 0.001, ****P < 0.0001 (unpaired t tests with Welch´s correction). Scale bar, 2 µm.

Figure 3: RPGRIP1L-deficient hiPSC-derived spinal organoids adopt the MN fate. **(A)** Schematic summary of the spinal 3D differentiation approach. Main neural progenitor and neuron populations obtained at each time point with their molecular markers are indicated below. Drugs used to induce or repress signaling pathways are indicated above. SB and LDN: SMAD antagonists SB-431542 and LDN-193189; CHIR: WNT agonist CHIR99021; SAG: SHH agonist; DAPT: NOTCH agonist; RA: Retinoic Acid. Modified after Maury et al., 2015. **(B)** Immunofluorescence analysis of MN progenitor formation and MN production in WT and *RPGRIP1L*$^{-/-}$ spinal organoids. OLIG2: marker of MN progenitors,

ISLET1/2: marker of postmitotic MNs. Quantifications show the relative OLIG2 and ISLET1/2 positive area per organoid over time. The scale bar represents a length of 50 µm. Data are shown as mean ± SEM. Asterisks denote statistical significance according to unpaired t tests with Welch´s correction (*P < 0.05) (WT: n=4; KO: n=4). **(C)** Heatmap of selected gene expressions from bulk RNAseq data of WT and RPGRIP1L-deficient spinal organoids over time. Log2(tpm+1)-graphs illustrate the dynamics of the expression levels of *DBX2*, *OLIG2*, *NKX6.1* and *NKX2.2* in WT and *RPGRIP1L*$^{-/-}$ organoids. Data are shown as mean ± SEM (WT: n=4; KO: n=3). **(D)** Immunofluorescence analysis of OLIG2-positive MN progenitors and NKX2.2-positive progenitors at day 9 and day 11 of spinal differentiation. WT and RPGRIP1L-deficient organoids are positive for OLIG2 at day 9 and OLIG2 is reduced at day 11. NKX2.2 is significantly increased at day 11 in RPGRIP1L-deficient organoids. The scale bar represents a length of 50 µm. Data are shown as mean ± SEM. Asterisks denote statistical significance according to unpaired t tests with Welch´s correction (*P < 0.05) (WT: n=4; KO: n=4). **(E)** Immunofluorescence analysis of TUBB3 at day 14 of spinal differentiation. WT and RPGRIP1L-deficient organoids express TUBB3 and no significant difference is present in the relative TUBB3 positive area per organoid at day 14. The scale bar represents a length of 100 µm. Data are shown as mean ± SEM (WT: n=4; KO: n=4). Log2(tpm+1) data from bulk RNASeq analyses show unaltered *TUBB3* expression between WT and RPGRIP1L-deficient organoids during differentiation. Data are shown as mean ± SEM (WT: n=4; KO: n=3).

Figure 4: RPGRIP1L-deficient hiPSC-derived neural progenitors harbor cilia and transduce SHH signaling. (A) Analysis of SHH target genes *GLI1* and *PTCH1*. Log2(tpm+1) data from bulk RNASeq analysis are displayed as mean ± SEM (WT: n=4; KO: n=3). **(B, C)** Immunofluorescence analysis of ciliary proteins on WT and RPGRIP1L-deficient spinal organoids at day 6 of differentiation. **(B)** Cilia are labeled by ARL13B in red and gamma-TUBULIN in grey. Cilia are present at apical sites pointing into inner cavities of the organoids. The scale bar represents a length of 300 µm. **(C)** Cilia are labeled by IFT81 in green. The scale bar represents 1 µm. The graph shows unaltered ciliary length in *RGPRIP1L*$^{-/-}$ organoids compared to WT. Data are shown as mean ± SEM (WT: n=4; KO: n=4). **(D)** Stimulated-Emission-Depletion (STED) images of WT and RPGRIP1L-deficient cilia at day 6 of differentiation. Cilia are labeled by ARL13B in green. RPGRIP1L is marked in red. The scale bar represents 1 µm. Quantification of RPGRIP1L was measured on confocal images. Data are shown as mean ± SEM. Asterisks denote statistical significance according to unpaired t tests with Welch´s correction (***P < 0.001) (WT: n=4; KO: n=4). **(E)** Immunofluorescence of WT and RPGRIP1L-deficient cilia on spinal organoids at day 6 of differentiation. Cilia are labeled by ARL13B in red and INPP5E in green. The basal body is labeled by gamma-TUBULIN in grey. The scale bar represents 1 µM. Quantifications show an unaltered amount of INPP5E but a decreased amount of ARL13B in RPGRIP1L-deficient cilia. Data are shown as mean ± SEM. Asterisks denote statistical significance according to unpaired t tests with Welch´s correction (***P < 0.001) (WT: n=4; KO: n=4). **(F)**

Immunofluorescence of WT and RPGRIP1L-deficient cilia on spinal organoids at day 6 of differentiation. Cilia are labeled by ARL13B in green and AC3 in red. The basal body is labeled by gamma-TUBULIN in grey. The scale bar represents 1 µm. Quantifications show a decreased amount of AC3 in RPGRIP1L-deficient cilia. Data are shown as mean ± SEM. Asterisks denote statistical significance according to unpaired t tests with Welch´s correction (***P < 0.001) (WT: n=4; KO: n=4).

Figure 5: RPGRIP1L-deficient spinal organoids show anterior-posterior patterning defects with MNs adopting hindbrain identity. (A) Heatmap showing *HOXA* and *HOXC* gene expression in WT and RPGRIP1L-deficient spinal organoids over time. The graph was generated from log2(tpm+1) files of bulk RNASeq analysis (WT: n=4; KO: n=3). **(B)** Log2(tpm+1) graphs show the expression profiles of selected HOX genes *HOXA5*, *HOXA7*, *HOXC4* and *HOXC8*. Data are shown as mean ± SEM (WT: n=4; KO: n=3). **(C)** Immunofluorescence of WT and RPGRIP1L-deficient spinal organoids at day 14 of differentiation. HOXA5 is stained in green and HOXC8 is labeled in red. The scale bar represents a length of 500 µm. Quantifications show the relative HOXA5 and HOXC8 positive areas per organoid. Data are shown as mean ± SEM. Asterisks denote statistical significance according unpaired t tests with Welch´s correction (***P < 0.001; ****P < 0.0001) (WT: n=4; KO: n=4). **(D)** Schematic overview about the four HOX gene clusters expressed from anterior to posterior positions. The black square indicates the genes that are expressed in WT spinal organoids. The red dotted square indicates the *HOX* genes expressed in RPGRIP1L-deficient spinal organoids. Schematic was created using BioRender. **(E-J)** Log2(tpm+1) graphs generated from bulk RNASeq analyses show the expression profiles of **(E)** *PHOX2B*, **(F)** *NKX2.9/NKX2.8*, **(G)** *TBX20*, **(H)** *PHOX2A,* **(I)** *EGR2/KROX20* and **(J)** *FGF3*. Data are shown as mean ± SEM (WT: n=4; KO: n=3).

Figure 6: Altered ciliogenesis on RPGRIP1L-deficient axial progenitors. (A) Immunofluorescence of WT and RPGRIP1L-deficient spinal organoids at day 4 of differentiation. CDX2 is stained in green. The scale bar represents a length of 250 µm. Quantifications show the relative CDX2 positive areas per organoid. Data are shown as mean ± SEM (WT: n=2; KO: n=2). **(B-F)** Log2(tpm+1) graphs generated from bulk RNASeq analyses show dynamic expression profiles of **(B)** *CDX2*, **(C)** *TBTX/Brachyury*, **(D)** *CDX1,* **(E)** *CDX4* and **(F)** *WNT5A*. Data are shown as mean ± SEM (WT: n=4; KO: n=3). **(E)** Immunofluorescence of cilia on WT and RPGRIP1L-deficient spinal organoids at day 4 of differentiation. Cilia are labeled in red by ARL13B in green by INPP5E. Cilia are present at apical sites pointing into inner cavities or the external environment in WT but not RPGRIP1L-deficient organoids. The scale bar represents a length of 300 µm. Magnified areas are indicated by yellow rectangles and magnified images are displayed on the right. The scale bar represents a length of 30 µm.

REFERENCES

1. Bachmann-Gagescu R, Dempsey J, Buldheroni S, Chen M, D'Arrigo S, Glass I, et al. Healthcare recommendations for Joubert syndrome. Am J Med Genet A. 2020;182(1):229-49.
2. Reiter J, Leroux M. Genes and molecular pathways underpinning ciliopathies. Nat Rev Mol Cell Biol. 2017;18(9):533-47.
3. Brancati F, Dallapiccola B, Valente E. Joubert Syndrome and related disorders. Orphanet J Rare Dis. 2010;5:20.
4. Goetz S, Anderson K. The primary cilium: a signalling centre during vertebrate development. Nat Rev Genet. 2010;11(5):331-44.
5. Spassky N, Han Y, Aguilar A, Strehl L, Besse L, Laclef C, et al. Primary cilia are required for cerebellar development and Shh-dependent expansion of progenitor pool. Dev Biol. 2008;317(1):246-59.
6. Andreu-Cervera A, Catala M, Schneider-Maunoury S. Cilia, ciliopathies and hedgehog-related forebrain developmental disorders. Neurobiol Dis. 2021;150:105236.
7. Andreu-Cervera A, Anselme I, Karam A, Laclef C, Catala M, Schneider-Maunoury S. The ciliopathy gene ftm/rpgrip1l controls mouse forebrain patterning via region-specific modulation of hedgehog/gli signaling. J Neurosci. 2019;39(13):2398-415.
8. Abdelhamed Z, Abdelmottaleb D, El-Asrag M, Natarajan S, Wheway G, Inglehearn C, et al. The ciliary Frizzled-like receptor Tmem67 regulates canonical Wnt/β-catenin signalling in the developing cerebellum via Hoxb5. Sci Rep. 2019;9(1):5446.
9. Lancaster M, Gopal D, Kim J, Saleem S, Silhavy J, Louie C, et al. Defective Wnt-dependent cerebellar midline fusion in a mouse model of Joubert syndrome. Nat Med. 2011;17(6):726-31.
10. Basten S, Giles R. Functional aspects of primary cilia in signaling, cell cycle and tumorigenesis. Cilia. 2013;2(1):6.
11. Delous M, Baala L, Salomon R, Laclef C, Vierkotten J, Tory K, et al. The ciliary gene RPGRIP1L is mutated in cerebello-oculo-renal syndrome (Joubert syndrome type B) and Meckel syndrome. Nat Genet. 2007;39(7):875-81.
12. Arts H, Doherty D, van Beersum S, Parisi M, Letteboer S, Gorden N, et al. Mutations in the gene encoding the basal body protein RPGRIP1L, a nephrocystin-4 interactor, cause Joubert syndrome. Nat Genet. 2007;39(7):882-8.
13. Doherty D, Parisi M, Finn L, Gunay-Aygun M, Al-Mateen M, Bates D, et al. Mutations in 3 genes (MKS3, CC2D2A and RPGRIP1L) cause COACH syndrome (Joubert syndrome with congenital hepatic fibrosis). J Med Genet. 2010;47(1):8-21.
14. Wolf M, Saunier S, O'Toole J, Wanner N, Groshong T, Attanasio M, et al. Mutational analysis of the RPGRIP1L gene in patients with Joubert syndrome and nephronophthisis. Kidney Int. 2007;72(12):1520-6.
15. Vierkotten J, Dildrop R, Peters T, Wang B, Rüther U. Ftm is a novel basal body protein of cilia involved in Shh signalling. Development. 2007;134(14):2569-77.
16. Besse L, Neti M, Anselme I, Gerhardt C, Rüther U, Laclef C, et al. Primary cilia control telencephalic patterning and morphogenesis via Gli3 proteolytic processing. Development. 2011;138(10):2079-88.
17. Garcia-Gonzalo F, Corbit K, Sirerol-Piquer M, Ramaswami G, Otto E, Noriega T, et al. A transition zone complex regulates mammalian ciliogenesis and ciliary membrane composition. Nat Genet. 2011;43(8):776-84.
18. Li C, Jensen V, Park K, Kennedy J, Garcia-Gonzalo F, Romani M, et al. MKS5 and CEP290 Dependent Assembly Pathway of the Ciliary Transition Zone. PLoS Biol. 2016;14(3):e1002416.

19. Shi X, Garcia Gr, Van De Weghe J, McGorty R, Pazour G, Doherty D, et al. Super-resolution microscopy reveals that disruption of ciliary transition-zone architecture causes Joubert syndrome. Nat Cell Biol. 2017;19(10):1178-88.
20. Benzing T, Schermer B. Transition zone proteins and cilia dynamics. Nat Genet. 2011;43(8):723-4.
21. Reiter J, Blacque O, Leroux M. The base of the cilium: roles for transition fibres and the transition zone in ciliary formation, maintenance and compartmentalization. EMBO Rep. 2012;13(7):608-18.
22. Williams C, Li C, Kida K, Inglis P, Mohan S, Semenec L, et al. MKS and NPHP modules cooperate to establish basal body/transition zone membrane associations and ciliary gate function during ciliogenesis. J Cell Biol. 2011;192(6):1023-41.
23. Wiegering A, Dildrop R, Kalfhues L, Spychala A, Kuschel S, Lier J, et al. Cell type-specific regulation of ciliary transition zone assembly in vertebrates. EMBO J. 2018;37(10):e97791.
24. Wiegering A, Dildrop R, Vesque C, Khanna H, Schneider-Maunoury S, Gerhardt C. Rpgrip1l controls ciliary gating by ensuring the proper amount of Cep290 at the vertebrate transition zone. Mol Biol Cell. 2021;32(8):675-89.
25. Omran H. NPHP proteins: gatekeepers of the ciliary compartment. J Cell Biol. 2010;190(5):715-7.
26. Sang L, Miller J, Corbit K, Giles R, Brauer M, Otto E, et al. Mapping the NPHP-JBTS-MKS protein network reveals ciliopathy disease genes and pathways. Cell. 2011;145(4):513-28.
27. Gerhardt C, Lier J, Burmühl S, Struchtrup A, Deutschmann K, Vetter M, et al. The transition zone protein Rpgrip1l regulates proteasomal activity at the primary cilium. J Cell Biol. 2015;210(1):115-33.
28. Struchtrup A, Wiegering A, Stork B, Rüther U, Gerhardt C. The ciliary protein RPGRIP1L governs autophagy independently of its proteasome-regulating function at the ciliary base in mouse embryonic fibroblasts. Autophagy. 2018;14(4):567-83.
29. Mahuzier A, Gaudé H, Grampa V, Anselme I, Silbermann F, Leroux-Berger M, et al. Dishevelled stabilization by the ciliopathy protein Rpgrip1l is essential for planar cell polarity. J Cell Biol. 2012;198(5):927-40.
30. Gerhardt C, Wiegering A, Leu T, Rüther U. Control of Hedgehog signalling by the cilia-regulated proteasome. J Dev Biol. 2016;4(3):27.
31. Willaredt M, Hasenpusch-Theil K, Gardner H, Kitanovic I, Hirschfeld-Warneken V, Gojak C, et al. A crucial role for primary cilia in cortical morphogenesis. J Neurosci. 2008;28(48):12887-900. .
32. Juric-Sekhar G, Adkins J, Doherty D, Hevner R. Joubert syndrome: brain and spinal cord malformations in genotyped cases and implications for neurodevelopmental functions of primary cilia. Acta Neuropathol. 2012;123(5):695-709.
33. ten Donkelaar H, Hoevenaars F, Wesseling P. A case of Joubert's syndrome with extensive cerebral malformations. Clin Neuropathol. 2000;19(2):85-93.
34. Briscoe J, Ericson J. Specification of neuronal fates in the ventral neural tube. J Curr Opin Neurobiol. 2001;11(1):43-9.
35. Bangs F, Anderson K. Primary Cilia and Mammalian Hedgehog Signaling. Cold Spring Harb Perspect Biol. 2017;9(5):pii: a028175.
36. Balaskas N, Ribeiro A, Panovska J, Dessaud E, Sasai N, Page K, et al. Gene regulatory logic for reading the Sonic Hedgehog signaling gradient in the vertebrate neural tube. Cell. 2012;148(1-2):273-84. .
37. Ribes V, Balaskas N, Sasai N, Cruz C, Dessaud E, Cayuso J, et al. Distinct Sonic Hedgehog signaling dynamics specify floor plate and ventral neuronal progenitors in the vertebrate neural tube. Genes Dev. 2010;24(11):1186-200.
38. Dessaud E, Ribes V, Balaskas N, Yang L, Pierani A, Kicheva A, et al. Dynamic assignment and maintenance of positional identity in the ventral neural tube by the morphogen sonic hedgehog. PLoS Biol. 2010;8(6):e1000382.
39. Dessaud E, Yang L, Hill K, Cox B, Ulloa F, Ribeiro A, et al. Interpretation of the sonic hedgehog morphogen gradient by a temporal adaptation mechanism. Nature. 2007;450(7170):717-20.

40. Jeong J, McMahon A. Growth and pattern of the mammalian neural tube are governed by partially overlapping feedback activities of the hedgehog antagonists patched 1 and Hhip1. Development. 2005;132(1):143-54.
41. Lek M, Dias J, Marklund U, Uhde C, Kurdija S, Lei Q, et al. A homeodomain feedback circuit underlies step-function interpretation of a Shh morphogen gradient during ventral neural patterning. Development. 2010;137(23):4051-60.
42. Huangfu D, Anderson K. Cilia and Hedgehog responsiveness in the mouse. Proc Natl Acad Sci U S A 2005;102(32):11325-30.
43. Huangfu D, Liu A, Rakeman A, Murcia N, Niswander L, Anderson K. Hedgehog signalling in the mouse requires intraflagellar transport proteins. Nature. 2003;426(6962):83-7.
44. Haycraft C, Banizs B, Aydin-Son Y, Zhang Q, Michaud E, Yoder B. Gli2 and Gli3 localize to cilia and require the intraflagellar transport protein polaris for processing and function. PLoS Genet. 2005;1(4):e53.
45. Liu A, Wang B, Niswander L. Mouse intraflagellar transport proteins regulate both the activator and repressor functions of Gli transcription factors. Development. 2005;132(13):3103-11.
46. Wichterle H, Lieberam I, Porter J, Jessell T. Directed differentiation of embryonic stem cells into motor neurons. Cell. 2002;110(3):385-97.
47. Duval N, Vaslin C, Barata T, Frarma Y, Contremoulins V, Baudin X, et al. BMP4 patterns Smad activity and generates stereotyped cell fate organization in spinal organoids. Development. 2019;146(14):dev175430.
48. Maury Y, Côme J, Piskorowski R, Salah-Mohellibi N, Chevaleyre V, Peschanski M, et al. Combinatorial analysis of developmental cues efficiently converts human pluripotent stem cells into multiple neuronal subtypes. Nature Biotechnology. 2015;33(1):89-96.
49. Mouilleau V, Vaslin C, Robert R, Gribaudo S, Nicolas N, Jarrige M, et al. Dynamic extrinsic pacing of the HOX clock in human axial progenitors controls motor neuron subtype specification. Development. 2021;146(6):dev194514.
50. Catala M, Teillet M, Le Douarin N. Organization and development of the tail bud analyzed with the quail-chick chimaera system. Mech Dev. 1995;51(1):51-65.
51. Wymeersch F, Huang Y, Blin G, Cambray N, Wilkie R, Wong F, et al. Position-dependent plasticity of distinct progenitor types in the primitive streak. Elife. 2016;5:e10042.
52. Wymeersch F, Wilson V, Tsakiridis A. Understanding axial progenitor biology in vivo and in vitro. Development. 2021;148(4):dev180612.
53. Cambray N, Wilson V. Two distinct sources for a population of maturing axial progenitors. Development. Development. 2007;134(15):2829-40.
54. Cambray N, Wilson V. Axial progenitors with extensive potency are localised to the mouse chordoneural hinge. Development. 2002;129(20):4855-66.
55. Jang S, Gunmit E, Wichterle H. Human-specific progenitor sub-domain contributes to extended neurogenesis and increased motor neuron production. bioRxiv. 2022.
56. Briscoe J, Sussel L, Serup P, Hartigan-O'Connor D, Jessell T, Rubenstein J, et al. Homeobox gene Nkx2.2 and specification of neuronal identity by graded Sonic hedgehog signalling. Nature. 1999;398(6728):622-7. .
57. Jensen V, Li C, Bowie R, Clarke L, Mohan S, Blacque O, et al. Formation of the transition zone by Mks5/Rpgrip1L establishes a ciliary zone of exclusion (CIZE) that compartmentalises ciliary signalling proteins and controls PIP2 ciliary abundance. EMBO J. 2015;34(20):2537-56.
58. Garcia-Gonzalo F, Phua S, Roberson E, Garcia Gr, Abedin M, Schurmans S, et al. Phosphoinositides Regulate Ciliary Protein Trafficking to Modulate Hedgehog Signaling. Dev Cell. 2015;34(4):400-9.
59. Mukhopadhyay S, Wen X, Ratti N, Loktev A, Rangell L, Scales S, et al. The ciliary G-protein-coupled receptor Gpr161 negatively regulates the Sonic hedgehog pathway via cAMP signaling. Cell. 2013;152(1-2):210-23.
60. Pal K, Hwang S, Somatilaka B, Badgandi H, Jackson P, DeFea K, et al. Smoothened determines β-arrestin-mediated removal of the G protein-coupled receptor Gpr161 from the primary cilium. J Cell Biol. 2016;212(7):861-75.

61. Chen C, Xu Q, Zhang Y, Davies B, Huang Y, Katzmann D, et al. Ciliopathy protein HYLS1 coordinates the biogenesis and signaling of primary cilia by activating the ciliary lipid kinase PIPKIγ. Sci Adv. 2021;7(26):eabe3401. .
62. Dasen J, Liu J, Jessell T. Motor neuron columnar fate imposed by sequential phases of Hox-c activity. Nature. 2003;425(6961):926-33.
63. Deschamps J, Duboule D. Embryonic timing, axial stem cells, chromatin dynamics, and the Hox clock. Genes Dev. 2017;31(14):1406-16.
64. Liu J, Laufer E, Jessell T. Assigning the positional identity of spinal motor neurons: rostrocaudal patterning of Hox-c expression by FGFs, Gdf11, and retinoids. Neuron. 2001;32(6):997-1012.
65. Pattyn A, Vallstedt A, Dias J, Samad O, Krumlauf R, Rijli F, et al. Coordinated temporal and spatial control of motor neuron and serotonergic neuron generation from a common pool of CNS progenitors. Genes Dev. 2003;17(6):729-37.
66. Dias J, Alekseenko Z, Jeggari A, Boareto M, Vollmer J, Kozhevnikova M, et al. A Shh/Gli-driven three-node timer motif controls temporal identity and fate of neural stem cells. Sci Adv. 2020;6(38):eaba8196.
67. Jarrar W, Dias J, Ericson J, Arnold H, Holz A. Nkx2.2 and Nkx2.9 are the key regulators to determine cell fate of branchial and visceral motor neurons in caudal hindbrain. PloS One. 2015;10(4):e0124408.
68. Pattyn A, Hirsch M, Goridis C, Brunet J. Control of hindbrain motor neuron differentiation by the homeobox gene Phox2b. Development. 2000;127(2):1349-58. .
69. Nordström U, Maier E, Jessell T, Edlund T. An early role for WNT signaling in specifying neural patterns of Cdx and Hox gene expression and motor neuron subtype identity. PLoS Biol. 2006;4(8):e252.
70. Guthrie S. Patterning and axon guidance of cranial motor neurons. Nat Rev Neurosci. 2007;8(1):859-71. .
71. Hirsch M, Glover J, Dufour H, Brunet J, Goridis C. Forced expression of Phox2 homeodomain transcription factors induces a branchio-visceromotor axonal phenotype. Dev Biol. 2007;303(2):687-702.
72. Ahn D, Ruvinsky I, Oates A, Silver L, Ho R. tbx20, a new vertebrate T-box gene expressed in the cranial motor neurons and developing cardiovascular structures in zebrafish. Mech Dev. 2000;95(1-2):253-8.
73. Kraus F, Haenig B, Kispert A. Cloning and expression analysis of the mouse T-box gene tbx20. Mech Dev. 2001;100(1):87-91.
74. Seitanidou T, Schneider-Maunoury S, Desmarquet C, Wilkinson D, Charnay P. Krox-20 is a key regulator of rhombomere-specific gene expression in the developing hindbrain. Mechanisms of Development. 1997;65:31-42.
75. Schneider-Maunoury S, Gilardi-Hebenstreit P, Charnay P. How to build a vertebrate hindbrain. Lessons from genetics. C R Acad Sci III. 1998;321(10):819-34. .
76. Frank D, Sela-Donenfeld D. Hindbrain induction and patterning during early vertebrate development. Cell Mol Life Sci. 2019;76(5):941-60.
77. Aragon F, Pujades C. FGF signaling controls caudal hindbrain specification through Ras-ERK1/2 pathway. BMC Dev Biol. 2009;9(61).
78. Walshe J, Maroon H, McGonnell I, Dickson C, Mason I. Establishment of hindbrain segmental identity requires signaling by FGF3 and FGF8. Curr Biol. 2002;12(13):1117-23.
79. Forlani S, Lawson K, Deschamps J. Acquisition of Hox codes during gastrulation and axial elongation in the mouse embryo. Development. 2003;130(16):3807-19.
80. Gouti M, Delile J, Stamataki D, Wymeersch F, Huang Y, Kleinjung J, et al. A Gene Regulatory Network Balances Neural and Mesoderm Specification during Vertebrate Trunk Development. Dev Cell. 2017;41(3):243-61.e7.
81. Henrique D, Abranches E, Verrier L, Storey K. Neuromesodermal progenitors and the making of the spinal cord. Development. 2015;142(17):2864-75. .
82. Kondoh H, Takada S, Takemoto T. Axial level-dependent molecular and cellular mechanisms underlying the genesis of the embryonic neural plate. Dev Growth Differ. 2016;58(5):427-36.

83. Wymeersch F, Skylaki S, Huang Y, Watson J, Economou C, Marek-Johnston C, et al. Transcriptionally dynamic progenitor populations organised around a stable niche drive axial patterning. Development. 2019;146(1):dev168161.
84. van den Akker E, Forlani S, Chawengsaksophak K, de Graaff W, Beck F, Meyer B, et al. Cdx1 and Cdx2 have overlapping functions in anteroposterior patterning and posterior axis elongation. Development. 2002;129(9):2181-93.
85. Marom K, Shapira E, Fainsod A. The chicken caudal genes establish an anterior-posterior gradient by partially overlapping temporal and spatial patterns of expression. Mech Dev. 1997;64(1-2):41-52.
86. Metzis V, Steinhauser S, Pakanavicius E, Gouti M, Stamataki D, Ivanovitch K, et al. Nervous System Regionalization Entails Axial Allocation before Neural Differentiation. Cell. 2018;175(4):1105-18.e17.
87. Chang J, Skromne I, Ho R. CDX4 and retinoic acid interact to position the hindbrain-spinal cord transition. Dev Biol. 2016;410(2):178-89.
88. Sturgeon K, Kaneko T, Biemann M, Gauthier A, Chawengsaksophak K, Cordes S. Cdx1 refines positional identity of the vertebrate hindbrain by directly repressing Mafb expression. Development. 2011;138(1):65-74.
89. Skromne I, Thorsen D, Hale M, Prince V, Ho R. Repression of the hindbrain developmental program by Cdx factors is required for the specification of the vertebrate spinal cord. Development. 2007;134(11):2147-58.
90. Joshi P, Darr A, Skromne I. CDX4 regulates the progression of neural maturation in the spinal cord. Dev Biol. 2019;449(2):132-42.
91. Amin S, Neijts R, Simmini S, van Rooijen C, Tan S, Kester L, et al. Cdx and T Brachyury Co-activate Growth Signaling in the Embryonic Axial Progenitor Niche. Cell Rep. 2016;17(12):3165-77.
92. Neijts R, Amin S, van Rooijen C, Deschamps J. Cdx is crucial for the timing mechanism driving colinear Hox activation and defines a trunk segment in the Hox cluster topology. Dev Biol. 2017;422(2):146-54.
93. Gouti M, Tsakiridis A, Wymeersch F, Huang Y, Kleinjung J, Wilson V, et al. In vitro generation of neuromesodermal progenitors reveals distinct roles for wnt signalling in the specification of spinal cord and paraxial mesoderm identity. PLoS Biol. 2014;12(8):e1001937.
94. Hackland J, Shelar P, Sandhu N, Prasad M, Charney R, Gomez G, et al. FGF Modulates the Axial Identity of Trunk hPSC-Derived Neural Crest but Not the Cranial-Trunk Decision. Stem Cell Reports. 2019;12(5):920-33.
95. Lippmann E, Williams C, Ruhl D, Estevez-Silva M, Chapman E, Coon J, et al. Deterministic HOX patterning in human pluripotent stem cell-derived neuroectoderm. Stem Cell Reports. 2015;14(4):632-44.
96. Mazzoni E, Mahony S, Peljto M, Patel T, Thornton S, McCuine S, et al. Saltatory remodeling of Hox chromatin in response to rostrocaudal patterning signals. Nature Neurosci. 2013;16(9):1191-8.
97. Young T, Deschamps J. Hox, Cdx, and anteroposterior patterning in the mouse embryo. J Curr Top Dev Biol. 2009;88:235-55.
98. Andre P, Song H, Kim W, Kispert A, Yang Y. Wnt5a and Wnt11 regulate mammalian anterior-posterior axis elongation. Development. 2015;142(8):1516-27.
99. Takada S, Stark K, Shea M, Vassileva G, McMahon J, McMahon A. Wnt-3a regulates somite and tailbud formation in the mouse embryo. Genes Dev. 1994;8(2):174-89.
100. Lancaster M, Schroth J, Gleeson J. Subcellular spatial regulation of canonical Wnt signalling at the primary cilium. Nat Cell Biol. 2011;13(6):700-7.
101. Simons M, Gloy J, Ganner A, Bullerkotte A, Bashkurov M, Krönig C, et al. Inversin, the gene product mutated in nephronophthisis type II, functions as a molecular switch between Wnt signaling pathways. Nat Genet. 2005;37(5):537-43.
102. Christensen S, Pedersen S, Satir P, Veland I, Schneider L. The primary cilium coordinates signaling pathways in cell cycle control and migration during development and tissue repair. Curr Top Dev Biol. 2008;85:261-301.

103. Veland I, Montjean R, Eley L, Pedersen L, Schwab A, Goodship J, et al. Inversin/Nephrocystin-2 is required for fibroblast polarity and directional cell migration. PLoS One. 2013;8(4):e60193.
104. Coschiera A, Yoshihara M, Lauter G, Sini Ezer S, Kere J, Swoboda P. Primary cilia promote the differentiation of human neurons through the WNT signaling pathway. bioRxiv. 2023:2023.04.06.535895.
105. Bangs F, Schrode N, Hadjantonakis A-K, Anderson K. Lineage specificity of primary cilia in the mouse embryo. Nat Cell Biol. 2015;17(2):113-22.
106. Soares H, Carmona B, Nolasco S, Viseu Melo L, Gonçalves J. Cilia Distal Domain: Diversity in Evolutionarily Conserved Structures. Cells. 2019;8(2):160.
107. Wang J, Thomas H, Thompson R, Waldrep S, Fogerty J, Song P, et al. Variable phenotypes and penetrance between and within different zebrafish ciliary transition zone mutants. Dis Model Mech. 2022;15(12):dmm049568.
108. Chang C, Zanini M, Shirvani H, Cheng J, Yu H, Feng C, et al. Atoh1 Controls Primary Cilia Formation to Allow for SHH-Triggered Granule Neuron Progenitor Proliferation. Developmental Cell. 2019;48(2):184-99.
109. Ong T, Trivedi N, Wakefield R, Frase S, Solecki D. Siah2 integrates mitogenic and extracellular matrix signals linking neuronal progenitor ciliogenesis with germinal zone occupancy. Nat Commun. 2020;11(1):5312.
110. Blaess S, Graus-Porta D, Belvindrah R, Radakovits R, Pons S, Littlewood-Evans A, et al. Beta1-integrins are critical for cerebellar granule cell precursor proliferation. J Neurosci. 2004;24(13):3402-12.
111. Akhshi T, Trimble W. A non-canonical Hedgehog pathway initiates ciliogenesis and autophagy. J Cell Biol 2021;220(1):e202004179.
112. Zhang K, Da Silva F, Seidl C, Wilsch-Bräuninger M, Herbst J, Huttner W, et al. Primary cilia are WNT-transducing organelles whose biogenesis is controlled by a WNT-PP1 axis. 2023;58(2):139-54.e8.
113. Miller A, Dasen J. Establishing and maintaining Hox profiles during spinal cord development. Semin Cell Dev Biol. 2024;152-153:44-57.
114. Afzal Z, Krumlauf R. Transcriptional Regulation and Implications for Controlling Hox Gene Expression. J Dev Biol. 2022;10(1):4.
115. Cooper F, Souilhol C, Haston S, Gray S, Boswell K, Gogolou A, et al. Notch signalling influences cell fate decisions and HOX gene induction in axial progenitors. Development. 2024;151(3):dev202098.
116. Wind M, Gogolou A, Manipur I, Granata I, Butler L, Andrews P, et al. Defining the signalling determinants of a posterior ventral spinal cord identity in human neuromesodermal progenitor derivatives. Development. 2021;148(6):dev194415.
117. Subramanian V, Meyer B, Gruss P. Disruption of the murine homeobox gene Cdx1 affects axial skeletal identities by altering the mesodermal expression domains of Hox genes. Cell. 1995;83(4):641-53.
118. Chawengsaksophak K, de Graaff W, Rossant J, Deschamps J, Beck F. Cdx2 is essential for axial elongation in mouse development. Proc Natl Acad Sci U S A. 2004;101(20):7641-5.
119. van Nes J, de Graaff W, Lebrin F, Gerhard M, Beck F, Deschamps J. The Cdx4 mutation affects axial development and reveals an essential role of Cdx genes in the ontogenesis of the placental labyrinth in mice. Development. 2006;133(3):419-28.
120. Chawengsaksophak K, James R, Hammond V, Köntgen F, Beck F. Homeosis and intestinal tumours in Cdx2 mutant mice. Nature. 1997;386(6620):84-7.
121. Davidson A, Zon L. The caudal-related homeobox genes cdx1a and cdx4 act redundantly to regulate hox gene expression and the formation of putative hematopoietic stem cells during zebrafish embryogenesis. Dev Biol. 2006;292(2):506-18.
122. Faas L, Isaacs H. Overlapping functions of Cdx1, Cdx2, and Cdx4 in the development of the amphibian Xenopus tropicalis. Dev Dyn. 2009;238(4):835-52.
123. Epstein M, Pillemer G, Yelin R, Yisraeli J, Fainsod A. Patterning of the embryo along the anterior-posterior axis: the role of the caudal genes. Development. 1997;124(19):3805-14.

124. Pownall M, Tucker A, Slack J, Isaacs H. eFGF, Xcad3 and Hox genes form a molecular pathway that establishes the anteroposterior axis in Xenopus. Development. 1996;122(12):3881-92.
125. Young T, Rowland J, van de Ven C, Bialecka M, Novoa A, Carapuco M, et al. Cdx and Hox genes differentially regulate posterior axial growth in mammalian embryos. Dev Cell. 2009;17(4):516-26.
126. Pilon N, Oh K, Sylvestre J, Bouchard N, Savory J, Lohnes D. Cdx4 is a direct target of the canonical Wnt pathway. Dev Biol. 2006;289(1):55-63.
127. Schyr R, Shabtai Y, Shashikant C, Fainsod A. Cdx1 is essential for the initiation of HoxC8 expression during early embryogenesis. FASEB J. 2012;26(6):2674-84.
128. Ocbina P, Tuson M, Anderson K. Primary cilia are not required for normal canonical Wnt signaling in the mouse embryo. PLoS One. 2009;4(8):e6839.
129. Blassberg R, Patel H, Watson T, Gouti M, Metzis V, Delás M, et al. Sox2 levels regulate the chromatin occupancy of WNT mediators in epiblast progenitors responsible for vertebrate body formation. Nat Cell Biol. 2022;24(5):633-44.
130. Niles K, Blaser S, Shannon P, Chitayat D. Fetal arthrogryposis multiplex congenita/fetal akinesia deformation sequence (FADS)-Aetiology, diagnosis, and management. Prenat Diagn. 2019;39(9):720-31.
131. Grotto S, Cuisset JM, Marret S, Drunat, Faure P, Audebert-Bellanger S, et al. Type 0 Spinal Muscular Atrophy: Further Delineation of Prenatal and Postnatal Features in 16 Patients. J Neuromuscul Dis. 2016;3(4):487-95.
132. Lufkin T, Mark M, Hart C, Dollé P, LeMeur M, Chambon P. Homeotic transformation of the occipital bones of the skull by ectopic expression of a homeobox gene. Nature. 1992;359(6398):835-41.
133. Salonen R, Paavola P. Meckel syndrome. J Med Genet. 1998;35(6):497-501.
134. Concordet J, Haeussler M. CRISPOR: intuitive guide selection for CRISPR/Cas9 genome editing experiments and screens. Nucleic Acids Res. 2018;26(W1):W242-W5. .
135. Roberson E, Dowdle W, Ozanturk A, Garcia-Gonzalo F, Li C, Halbritter J, et al. TMEM231, mutated in orofaciodigital and Meckel syndromes, organizes the ciliary transition zone. J Cell Biol. 2015;209(1):129-42.
136. Yee L, Garcia-Gonzalo F, Bowie R, Li C, Kennedy J, Ashrafi K, et al. Conserved Genetic Interactions between Ciliopathy Complexes Cooperatively Support Ciliogenesis and Ciliary Signaling. PLoS Genet. 2015;11(11):e1005627.
137. Dobin A, Davis C, Schlesinger F, Drenkow J, Zaleski C, Jha S, et al. STAR: ultrafast universal RNA-seq aligner. Bioinformatics. 2013;29(1):15-21.
138. Ewels P, Magnusson M, Lundin S, Käller M. MultiQC: summarize analysis results for multiple tools and samples in a single report. Bioinformatics. 2016;32(19):3047-48.
139. Liao Y, Smyth G, Shi W. featureCounts: an efficient general purpose program for assigning sequence reads to genomic features. Bioinformatics. 2014;30(7):923-30.
140. Ramírez F, Ryan D, Grüning B, Bhardwaj V, Kilpert F, Richter A, et al. deepTools2: a next generation web server for deep-sequencing data analysis. Nucleic Acids Res. 2016;44(W1):W160-W5.
141. Love M, Huber W, Anders S. Moderated estimation of fold change and dispersion for RNA-seq data with DESeq2. Genome Biol. 2014;15(12):550.
142. Zink R, Wolfinger R, Mann G. Summarizing the incidence of adverse events using volcano plots and time intervals. Clin Trials. 2013;10(3):398-406.
143. Young M, Wakefield M, Smyth G, Oshlack A. Gene ontology analysis for RNA-seq: accounting for selection bias. Genome Biol. 2010;11(2):R14.
144. Alhamdoosh M, Ng M, Wilson N, Sheridan J, Huynh H, Wilson M, et al. Combining multiple tools outperforms individual methods in gene set enrichment analyses. Bioinformatics. 2017;33(3):414-24.

Figure 1

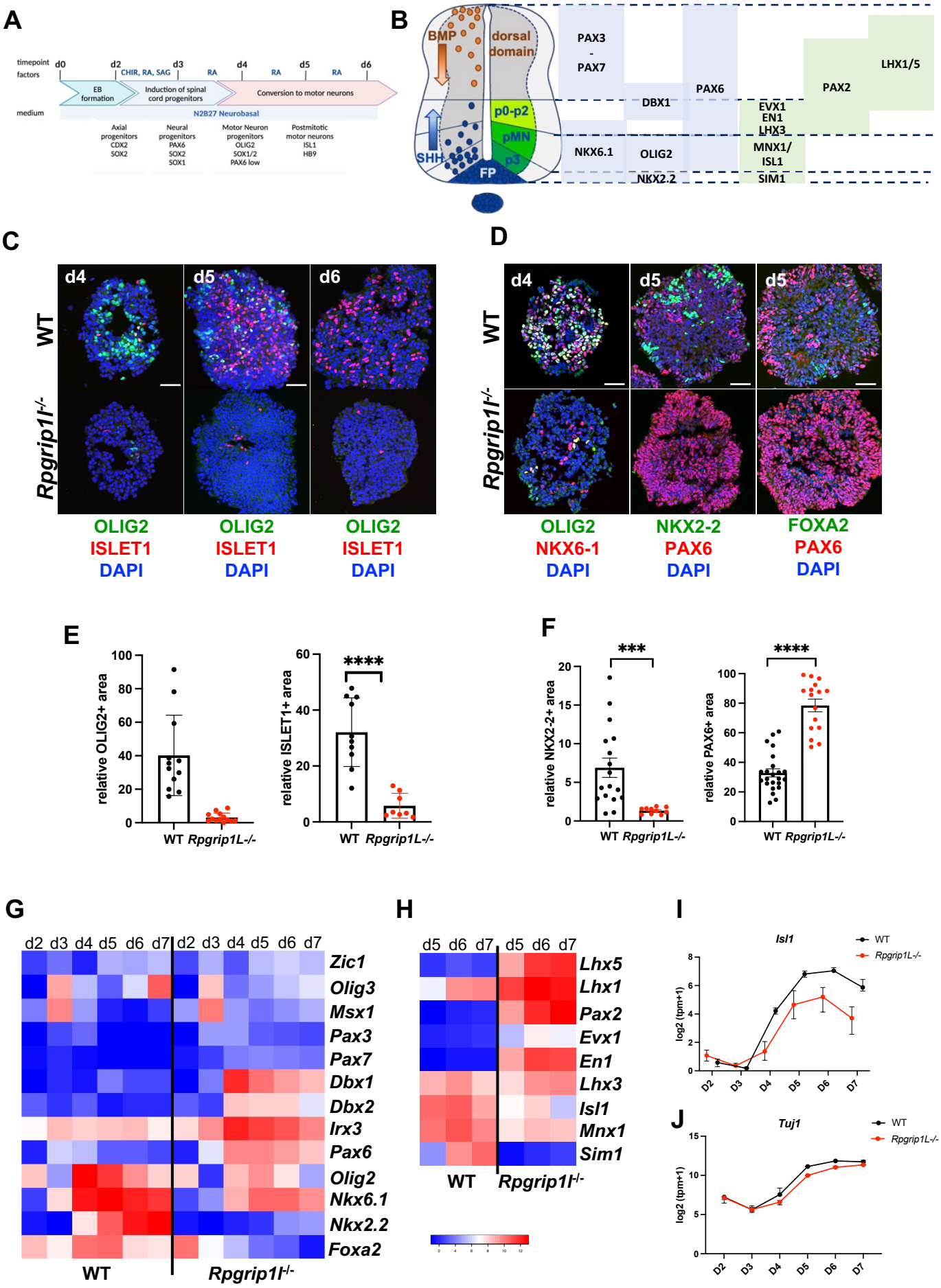
A
timepoint
factors
d0
d2
d3
d4
d5
d6
CHIR, RA, SAG
RA
RA
RA
EB formation
Induction of spinal cord progenitors
Conversion to motor neurons
medium
N2B27 Neurobasal
Axial progenitors CDX2 SOX2
Neural progenitors PAX6 SOX2 SOX1
Motor Neuron progenitors OLIG2 SOX1/2 PAX6 low
Postmitotic motor neurons ISL1 HB9
B
BMP
dorsal domain
SHH
FP
p0-p2
pMN
p3
PAX3 - PAX7
DBX1
PAX6
NKX6.1
OLIG2
NKX2.2
EVX1 EN1 LHX3
MNX1/ ISL1
SIM1
PAX2
LHX1/5
C
d4
d5
d6
WT
Rpgrip1l-/-
OLIG2
ISLET1
DAPI
D
NKX6-1
NKX2-2
PAX6
FOXA2
E
relative OLIG2+ area
relative ISLET1+ area
****
WT
Rpgrip1L-/-
F
relative NKX2-2+ area
relative PAX6+ area
***
G
d2 d3 d4 d5 d6 d7
Zic1
Olig3
Msx1
Pax3
Pax7
Dbx1
Dbx2
Irx3
Pax6
Olig2
Nkx6.1
Nkx2.2
Foxa2
H
Lhx5
Lhx1
Pax2
Evx1
En1
Lhx3
Isl1
Mnx1
Sim1
I
Isl1
log2 (tpm+1)
D2
D3
D4
D5
D6
D7
J
Tuj1

Figure 2

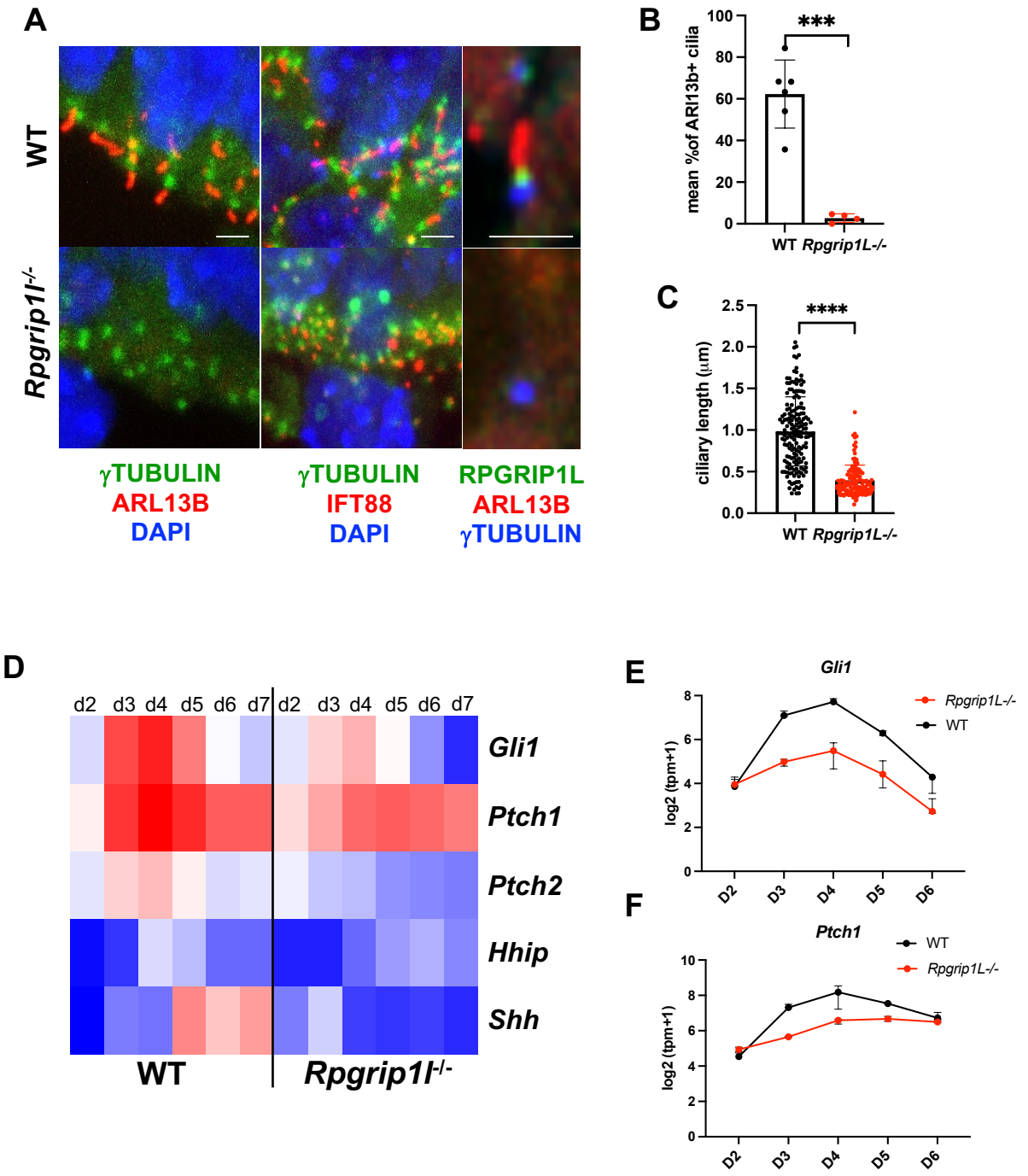
A
WT
Rpgrip1l-/-
γTUBULIN
ARL13B
DAPI
γTUBULIN
IFT88
DAPI
RPGRIP1L
ARL13B
γTUBULIN
B
mean %of ARl13b+ cilia
***
WT
Rpgrip1L-/-
C
ciliary length (μm)
****
WT
Rpgrip1L-/-
D
d2 d3 d4 d5 d6 d7 d2 d3 d4 d5 d6 d7
Gli1
Ptch1
Ptch2
Hhip
Shh
WT
Rpgrip1l-/-
E
Gli1
Rpgrip1L-/-
WT
log2 (tpm+1)
D2 D3 D4 D5 D6
F
Ptch1
WT
Rpgrip1L-/-
log2 (tpm+1)
D2 D3 D4 D5 D6

Figure 3

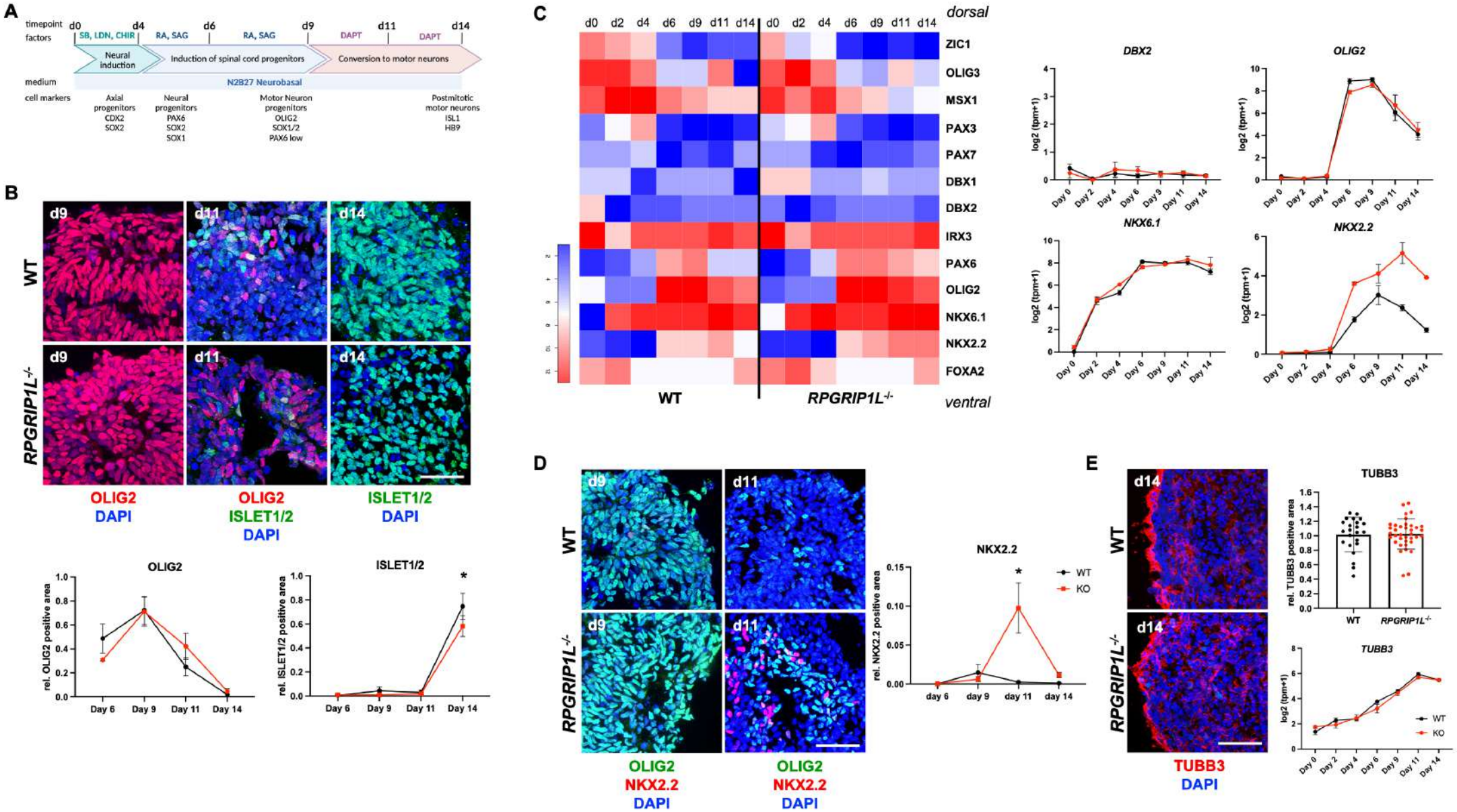
A
timepoint
factors
d0
d4
d6
d9
d11
d14
SB, LDN, CHIR
RA, SAG
RA, SAG
DAPT
DAPT
Neural induction
Induction of spinal cord progenitors
Conversion to motor neurons
medium
N2B27 Neurobasal
cell markers
Axial progenitors CDX2 SOX2
Neural progenitors PAX6 SOX2 SOX1
Motor Neuron progenitors OLIG2 SOX1/2 PAX6 low
Postmitotic motor neurons ISL1 HB9
B
WT
RPGRIP1L-/-
d9
d11
d14
OLIG2 DAPI
OLIG2 ISLET1/2 DAPI
ISLET1/2 DAPI
OLIG2
rel. OLIG2 positive area
ISLET1/2
rel. ISLET1/2 positive area
Day 6
Day 9
Day 11
Day 14
C
dorsal
ventral
ZIC1
OLIG3
MSX1
PAX3
PAX7
DBX1
DBX2
IRX3
PAX6
OLIG2
NKX6.1
NKX2.2
FOXA2
WT
RPGRIP1L-/-
DBX2
OLIG2
NKX6.1
NKX2.2
log2 (tpm+1)
Day 0
Day 2
Day 4
Day 6
Day 9
Day 11
Day 14
D
WT
RPGRIP1L-/-
d9
d11
OLIG2 NKX2.2 DAPI
NKX2.2
rel. NKX2.2 positive area
WT
KO
day 6
day 9
day 11
day 14
E
WT
RPGRIP1L-/-
d14
TUBB3 DAPI
TUBB3
rel. TUBB3 positive area
WT
RPGRIP1L-/-
TUBB3
log2 (tpm+1)
WT
KO

Figure 4

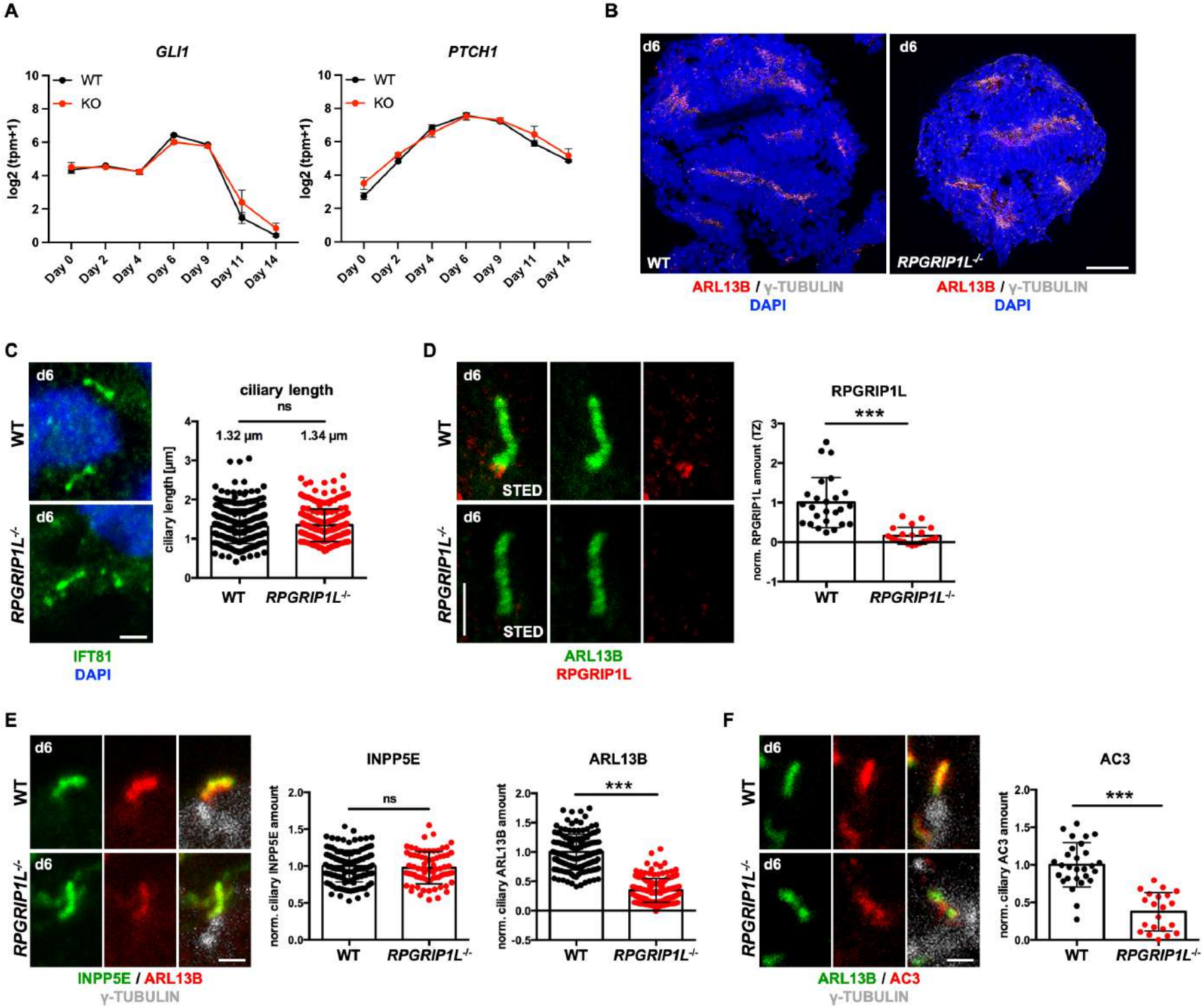
A
GLI1
PTCH1
WT
KO
log2 (tpm+1)
Day 0
Day 2
Day 4
Day 6
Day 9
Day 11
Day 14
B
d6
WT
RPGRIP1L-/-
ARL13B / γ-TUBULIN
DAPI
C
d6
WT
RPGRIP1L-/-
IFT81
DAPI
ciliary length
ns
1.32 µm
1.34 µm
ciliary length [µm]
D
STED
RPGRIP1L
***
norm. RPGRIP1L amount (TZ)
ARL13B
RPGRIP1L
E
INPP5E / ARL13B
γ-TUBULIN
INPP5E
ARL13B
norm. ciliary INPP5E amount
norm. ciliary ARL13B amount
F
AC3
norm. ciliary AC3 amount
ARL13B / AC3
γ-TUBULIN

Figure 5

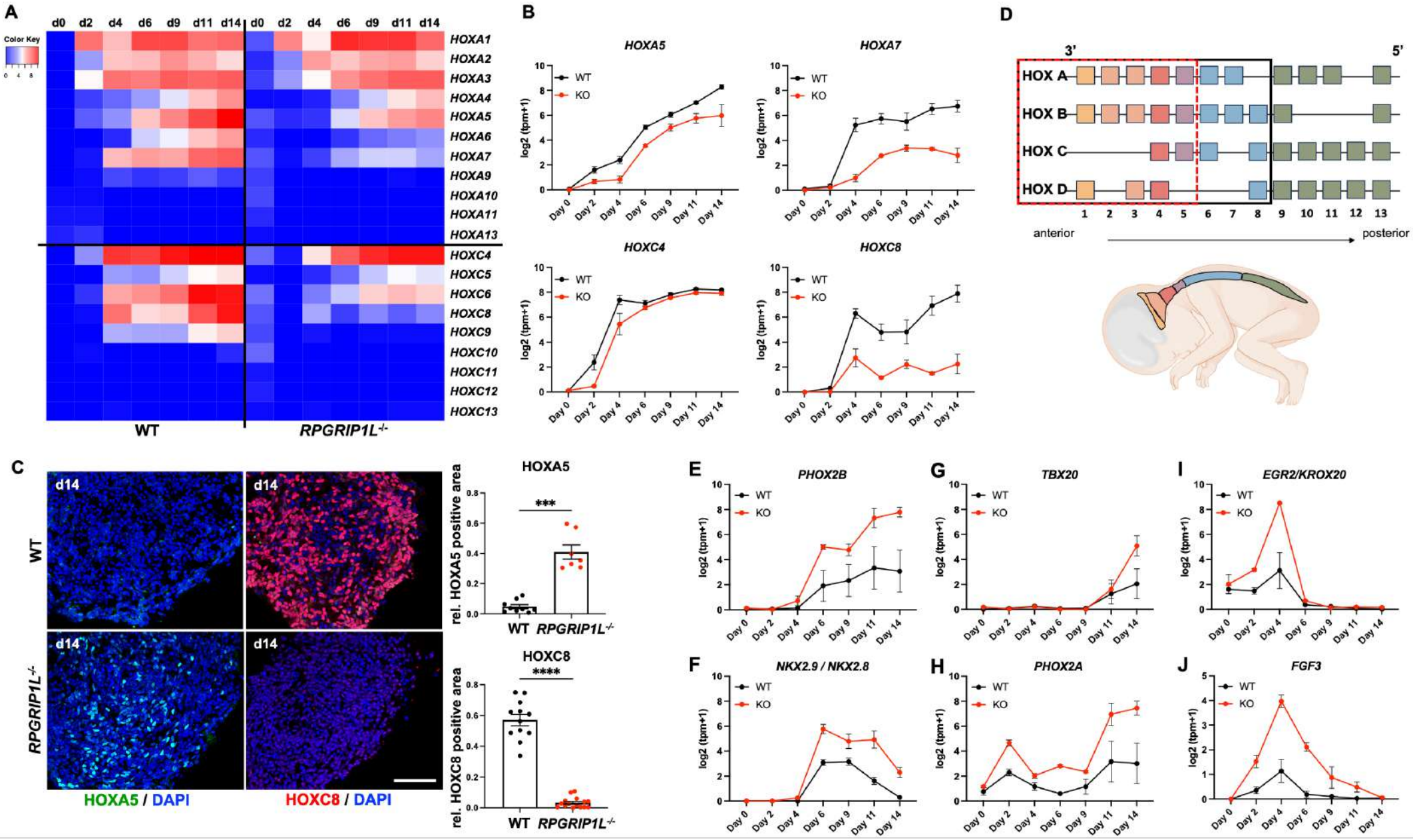
A
d0 d2 d4 d6 d9 d11 d14 d0 d2 d4 d6 d9 d11 d14
Color Key
HOXA1
HOXA2
HOXA3
HOXA4
HOXA5
HOXA6
HOXA7
HOXA9
HOXA10
HOXA11
HOXA13
HOXC4
HOXC5
HOXC6
HOXC8
HOXC9
HOXC10
HOXC11
HOXC12
HOXC13
WT
RPGRIP1L-/-
B
HOXA5
HOXA7
HOXC4
HOXC8
WT
KO
log2 (tpm+1)
Day 0 Day 2 Day 4 Day 6 Day 9 Day 11 Day 14
D
3'
5'
HOX A
HOX B
HOX C
HOX D
1 2 3 4 5 6 7 8 9 10 11 12 13
anterior
posterior
C
d14
WT
RPGRIP1L-/-
HOXA5 / DAPI
HOXC8 / DAPI
HOXA5
rel. HOXA5 positive area
***
WT RPGRIP1L-/-
HOXC8
rel. HOXC8 positive area
****
E
PHOX2B
F
NKX2.9 / NKX2.8
G
TBX20
H
PHOX2A
I
EGR2/KROX20
J
FGF3

Figure 6

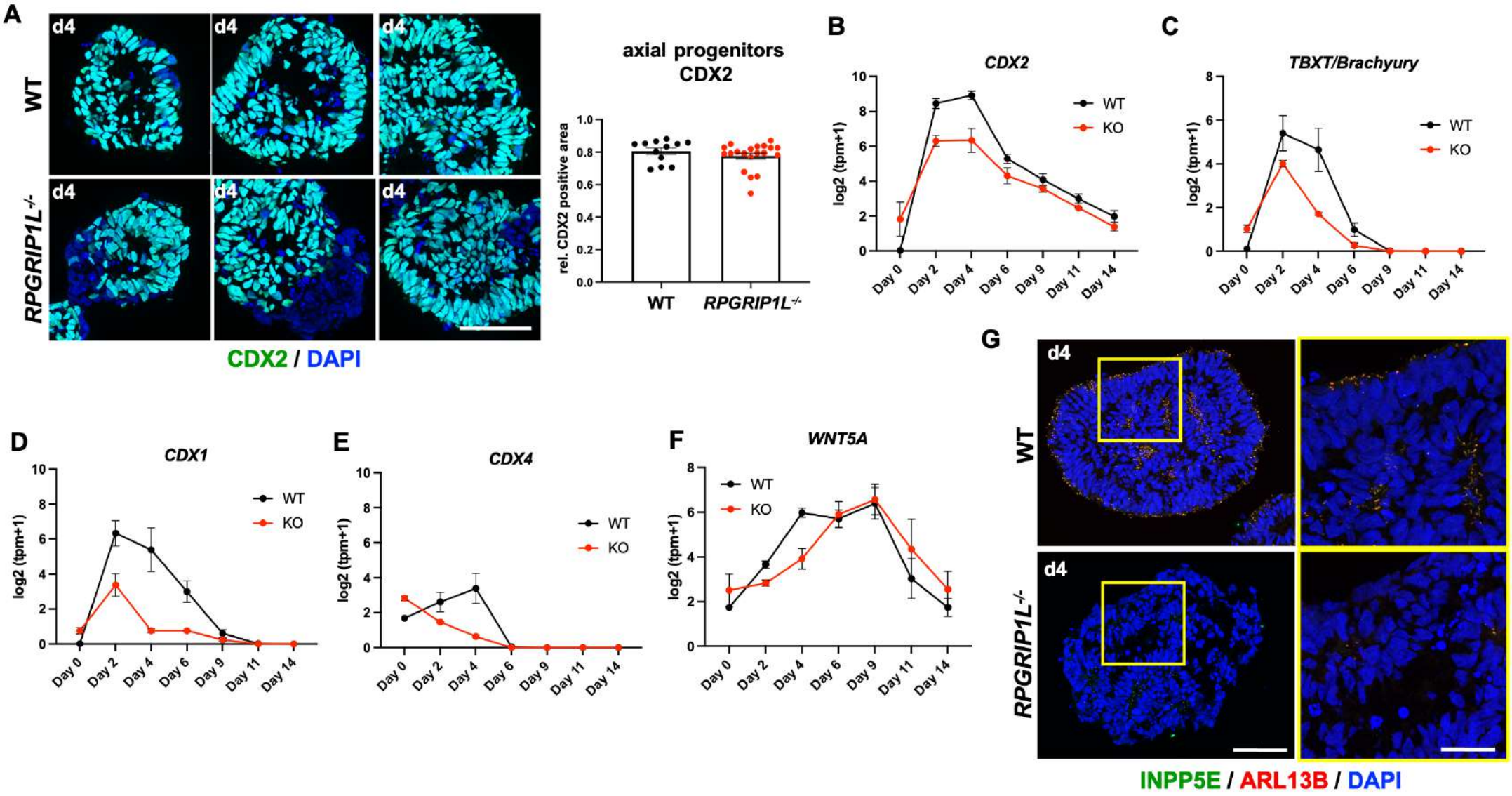
A
d4
WT
RPGRIP1L-/-
CDX2 / DAPI
axial progenitors
CDX2
rel. CDX2 positive area
WT
RPGRIP1L-/-
B
CDX2
log2 (tpm+1)
WT
KO
Day 0
Day 2
Day 4
Day 6
Day 9
Day 11
Day 14
C
TBXT/Brachyury
D
CDX1
E
CDX4
F
WNT5A
G
INPP5E / ARL13B / DAPI